AFRL-SN-HS-TR-2005-003

ULTRA-WIDEBAND SIGNALS FOR TARGET DETECTION IN FOLIAGE

Kung-Hau Ding
John K. Schindler
Kristopher T. Kim
Leonid I. Perlovsky
J. Leon Poirier
Elihu J. Tichovolsky
Bertus Weijers

In-House Technical Report: January 2002 – March 2003

AIR FORCE RESEARCH LABORATORY
Sensors Directorate
Electromagnetics Technology Division
80 Scott Drive
Hanscom AFB MA 01731-2909

TECHNICAL REPORT

Ultra-Wideband Signals for Target Detection in Foliage

Unlimited, Statement A

NOTICE

USING GOVERNMENT DRAWINGS, SPECIFICATIONS, OR OTHER DATA INCLUDED IN THIS DOCUMENT FOR ANY PURPOSE OTHER THAN GOVERNMENT PROCUREMENT DOES NOT IN ANY WAY OBLIGATE THE US GOVERNMENT. THE FACT THAT THE GOVERNMENT FORMULATED OR SUPPLIED THE DRAWINGS, SPECIFICATIONS, OR OTHER DATA DOES NOT LICENSE THE HOLDER OR ANY OTHER PERSON OR CORPORATION; OR CONVEY ANY RIGHTS OR PERMISSION TO MANUFACTURE, USE, OR SELL ANY PATENTED INVENTION THAT MAY RELATE TO THEM.

THIS TECHNICAL REPORT HAS BEEN REVIEWED AND IS APPROVED FOR PUBLICATION.

//signature//

Kung-Hau Ding
Project Manager, Electromagnetics Scattering Branch

//signature//

Bertus Weijers
Chief, Electromagnetics Scattering Branch

//signature//

Michael N. Alexander
Technical Advisor
Electromagnetics Technology Division

REPORT DOCUMENTATION PAGE

Form Approved
OMB No. 0704-0188

1. REPORT DATE *(DD-MM-YYYY)* 01-1-2004	IN-HOUSE
3. DATES COVERED *(From - To)* JAN 2002 – Mar 2003	
4. TITLE AND SUBTITLE Ultra-Wideband Signals for Target Detection in Foliage	**5a. CONTRACT NUMBER**
	5b. GRANT NUMBER
	5c. PROGRAM ELEMENT NUMBER 612304
6. AUTHOR(S) Kung-Hau Ding, John K. Schindler, Kristopher T. Kim, Leonid I. Perlovsky, J. Leon Poirier, Elihu J. Tichovolsky and Bertus Weijers	**5d. PROJECT NUMBER** 2304
	5e. TASK NUMBER HE
	5f. WORK UNIT NUMBER 01
7. PERFORMING ORGANIZATION NAME(S) AND ADDRESS(ES) Electromagnetic Scattering Branch, Sensors Directorate, 80 Scott Drive, Hanscom AFB, MA 01731-2909 ARCON Corporation, 260 Bear Hill Road, Waltham, MA 02154 Veridian Corporaiton, 3040 Williams Drive, Suite 200, Fairfax, VA 22031	**8. PERFORMING ORGANIZATION REPORT**
9. SPONSORING / MONITORING AGENCY NAME(S) AND ADDRESS(ES) Electromagnetics Technology Division Sensors Directorate Air Force Research Laboratory 80 Scott Drive Hanscom AFB MA 01731-2909	**10. SPONSOR/MONITOR'S ACRONYM(S)** AFRL/SNHE
	11. SPONSOR/MONITOR'S REPORT NUMBER(S) AFRL-SN-HS-TR-2005-003

12. DISTRIBUTION / AVAILABILITY STATEMENT
APPROVED FOR PUBLIC RELEASE; DISTRIBUTION UNLIMITED

13. SUPPLEMENTARY NOTES

14. ABSTRACT

In this report we have demonstrated the properties of precursor-like waveforms that are important if these waveforms are to be considered for radar detection of targets embedded in foliage. These properties are: (1) Precursor-like waveforms are greatly attenuated in comparison with the excitation signal due to the fact that the precursor formation medium must be highly dispersive and has a rapidly increasing attenuation with frequency. The precursor-like waveforms are formed from sideband energy of the excitation signal in a medium that has greatly attenuated the carrier frequency and upper sideband energy. (2) Precursor-like behavior is exhibited only after propagating through several skin depths of the medium at the carrier frequency of excitation. This insures that the carrier and upper sidebands of the excitation are greatly attenuated. (3) Precursor-like behavior of the response waveform persists with target scattering when the target is embedded in a dispersive, Debye medium. Target scattering attenuates low frequency portions of the spectrum due to Rayleigh scattering from the target at very low frequencies. As long as there remains a substantial portion of the response spectrum that is equalized over a band between the Rayleigh scattering and the carrier frequency, the precursor-like behavior of the time response will be observed. In this case, the duration of the precursors will be increased due to the low frequency bandwidth limitations imposed on the spectrum by the target Rayleigh scattering. (4) Foliage is weakly dispersive when compared to water and results in weak or negligible precursor formation in the coherent or ensemble average waveform at reasonable foliage depths. According to the experimental observations of trees and their wood fibers, as modeled by Brown and Curry, wood conductivity due to the ionic conductivity of salts and minerals in the tree sap dominates Debye losses. The component of loss associated with the Debye polarizability resonance is sensitive to the water content of the wood, the resonant frequency varying between 10 and 20 GHz, depending on the temperature of the wood. Since conductivity dominates, we lose much of the Debye behavior that is the source of precursors in water.

15. SUBJECT TERMS
Precursor, Ultra-Wideband Signals, Foliage clutter, Debye behavior

16. SECURITY CLASSIFICATION OF:			**17.LIMITATION OF ABSTRACT**	**18.NUMBER OF PAGES**	**19a. NAME OF RESPONSIBLE PERSON** Dr. Kung-Hau Ding
a. REPORT Unclassified	**b. ABSTRACT** Unclassified	**c.THIS PAGE** Unclassified	UU	63	**19b. TELEPHONE NUMBER** *(include area code)* *781-377-1730*

Standard Form 298 (Rev. 8-98)
Prescribed by ANSI Std. Z39.18

Ultra-Wideband Signals for Target Detection in Foliage

Contents

Illustrations

Summary

The goal of this study was to determine if precursors are formed when an ultra wideband (UWB) signal propagates in a foliage canopy and whether such a waveform offers advantages in detecting targets in foliage. We used linear system theory and Fourier analysis in our approach. This approach is rigorous and, unlike more cumbersome mathematical approaches, gives a clear insight into the process of precursor formation and propagation.

We first investigate UWB propagation in water characterized by a Debye model permittivity. Then we add a target in the water medium to more closely simulate the radar problem. We then extend our analysis to a foliage canopy characterized by an effective permittivity based on the measured complex dielectric constant of live tree wood.

Our analyses show how and why precursors are formed in water but not in foliage. Furthermore, we show that, for typical radar propagation paths, the signal-to-white noise ratio can always be optimized with a properly chosen narrowband lower frequency signal instead of an UWB waveform. Our specific findings include: (1) Precursor-like waveforms are greatly attenuated in comparison with the excitation signal due to the fact that the precursor formation medium must be highly dispersive and has a rapidly increasing attenuation with frequency. The precursor-like waveforms are formed from lower sideband energy of the excitation signal in a medium that has greatly attenuated the carrier frequency and upper sideband energy. (2) Precursor-like behavior is exhibited only after propagating through several skin depths of the medium at the carrier frequency of excitation. This insures that the carrier and upper sidebands of the excitation are greatly attenuated. (3) Precursor-like behavior of the response waveform persists with target scattering when the target is embedded in a dispersive, Debye medium. Target scattering attenuates low frequency portions of the spectrum due to Rayleigh scattering from the target at very low frequencies. As long as there remains a substantial portion of the response spectrum that is equalized over a pass band between the Rayleigh scattering and the carrier frequency, the precursor-like behavior of the time response will be observed. In this case, the duration of the precursors will be increased due to the low frequency bandwidth limitations imposed on the spectrum by the target Rayleigh scattering. (4) Foliage is weakly dispersive and results in weak or negligible precursor formation in the coherent or ensemble average waveform at reasonable foliage depths. According to the experimental observations of trees and their wood fibers, as modeled by Brown and Curry, wood conductivity losses due to the ionic conductivity of salts and minerals in the tree sap dominates Debye losses. The component of loss associated with the Debye polarizability resonance is sensitive to the water content of the wood, the resonant frequency varying between 10 and 20 GHz, depending on the temperature of the wood. Since conductivity dominates, we lose much of the Debye behavior that is the source of precursors in water.

1. Introduction

Foliage Penetration (FOPEN) radar is a critical need for Air Force tactical missions. Besides its all-weather, day-night capability, FOPEN using Synthetic Aperture Radar (SAR), operating at relatively lower electromagnetic frequencies (25 MHz to 1 GHz), offers the capability for penetrating foliage and imaging targets hidden within tree lines and deep foliage. FOPEN SAR is an important technique to detect hostile targets hidden in foliage.

The foliage penetration depth of radar varies with foliage conditions, such as moisture content, tree density, tree height, etc., and the radar's operating frequency, grazing angle, and polarization. Critical analyses and experimental measurements have both demonstrated the capability of VHF and UHF signals to penetrate foliage canopies. The attenuation coefficient is less than 1 dB/m within this range of wavelengths [Mower, 1988; Bessette and Ayasli, 2001]. However, the target detection performance of a FOPEN VHF/UHF imaging radar is hampered by high false alarm rates due to many image pixels from clutter that have radar responses comparable to those of military targets. Clutter mitigation and false alarm reduction are the challenging issues for practicable low false alarm FOPEN target detection.

Until recently, algorithms to effectively process FOPEN radar signals for clutter-target discrimination were not available. Change detection offers the capability for detecting scene changes between imaging passes. To detect scene changes, two SAR images are taken of the same scene, but at different times. These images have to be geometrically registered to align the same pixels in each image. After the images are geo-registered, pixels are either coherently or non-coherently subtracted. The resultant difference image can reveal minor changes such as those caused by vehicular movement. While this technique is currently the most effective FOPEN false alarm mitigation technique, it does increase mission risk due to the requirement for at least two flight passes over the same area with nearly the same flight path. This change detection technique also has the disadvantage of requiring longer image processing time and will not detect targets hidden in deep foliage that have not moved between radar passes. A robust algorithm for single-pass FOPEN SAR target detection would be of great military value.

Ultra wideband (UWB) radar technology has been proposed for improved FOPEN target detection and classification. UWB radars are characterized by very wide bandwidths (>25%) and the commensurate fine range resolution. Recent research funded by the Mathematics and Space Sciences Directorate of the Air Force Office of Scientific Research (AFOSR/NM) has proposed the use of UWB FOPEN radars using "precursor" waveforms [Nachman, 2001], (the Brillouin precursor [Oughstun, 2001]), to improve electromagnetic wave penetration through foliage. The precursor is an ultra wideband waveform that has been distorted due to propagation through a linear, homogeneous, causal, and dispersive medium. The distortion is due to the dispersive characteristics of the medium that causes some frequency regions to be absorbed more than others. Precursors have been studied extensively for several decades [Sommerfeld, 1914; Brillouin, 1914; Stratton, 1942; Brillouin, 1960; Jackson, 1975, Barrett, 1990; Oughstun and Sherman, 1995]. There are two types of precursors: Sommerfeld and Brillouin precursors. The Sommerfeld precursor is due to the high frequency components contained in the spectrum of excitation signal, which travels with the speed of light but attenuates exponentially when propagating into the medium. The Brillouin precursor is due to the low frequency components contained in the spectrum of excitation signal. The amplitude of Brillouin precursor has been found to decay non-exponentially such that it can penetrate deeper into the lossy medium than the Sommerfeld precursor and the main body of the excitation signal [Oughstun, 2001; Nachman, 2001]. This last property is the feature that the AFOSR work cited above is planning to exploit to achieve foliage penetration.

The idea of using the Brillion precursor waveform for FOPEN radars motivates the present study. The goal of the study is to determine if precursors are formed when an UWB signal propagates in a foliage canopy and whether such a waveform offers advantages in detecting targets hidden in foliage. We use linear system theory and Fourier analysis. This approach is rigorous and, unlike more cumbersome mathematical approaches, is intuitively satisfying. It gives clear insight into the process of precursor formation and on their propagation in any medium. We first investigate, in Section 2, UWB propagation in water characterized by a Debye model permittivity. In Section 3, a target is added behind a water slab to more closely portray the radar scenario. In Section 4, we extend the analysis to a foliage canopy characterized by an effective permittivity based on the measured complex dielectric constant of live tree wood and on the propagation through a medium of randomly oriented obstacles [Brown-Curry, 1980/ 1982]. Section 5 discusses the results of our study.

2. Ultra-Wideband Signal Propagation in Dispersive Water Medium

Water is a well-studied lossy and dispersive medium. It is an important component of foliage, such as leaves, branches, trunks, and soil, whose dielectric properties account for most of the absorption and scattering of electromagnetic energy in foliage. Transient signal propagation in a linear, homogeneous, dispersive medium has been studied for several decades [Sommerfeld, 1914; Brillouin, 1914; Stratton, 1942; Brillouin, 1960; Jackson, 1975, Barrett, 1990; Oughstun and Sherman, 1995]. The most studied media have a Lorenzian dispersion model [Oughstun, 1991; Oughstun and Laurens, 1991; Oughstun and Sherman 1995; Smith and Oughstun, 1998] often used in solid-state physics. The mathematics of complex variables (saddle points) and approximate asymptotic methods employed to treat the subject hide the nature of the fundamental precursor formation and propagation process. In this section we revisit the topic of ultra-wideband pulse propagation in a dispersive water medium using a Debye model [Albanese et al., 1989; Blaschak and Franzen, 1995; Roberts and Peropoulos, 1996], adopting a simpler, but rigorous, approach based on Maxwell's equations [Kong, 1990], linear system theory [Oppenheim et al., 1997], and Fourier analysis [Papoulis, 1987]. This approach gives a simple intuitive physical explanation for the formation and propagation of precursor-like waveforms in lossy and dispersive dielectric media.

2.1 Wave Propagation Model of a Half-Space Dispersive Medium

As shown in Figure 2.1, we consider a horizontally polarized (TE) electromagnetic plane wave incident at angle θ_i on a half-space of dielectric medium at $z = 0$. The upper half-space is air, characterized by the wave number $k_0 = \omega\sqrt{\mu_0\varepsilon_0}$, with $\omega = 2\pi f$ being the angular frequency, and μ_0 and ε_0 respectively the permeability and permittivity of free-space. The lower half-space is homogeneous and is characterized by the wave number $k_1 = \omega\sqrt{\mu_1\varepsilon_1}$, with μ_1 and ε_1 respectively permeability and permittivity of the lower region. Notice that $\mu_1 = \mu_0$ is a constant, while $\varepsilon_1 = \varepsilon_1(\omega)$ is a function of frequency.

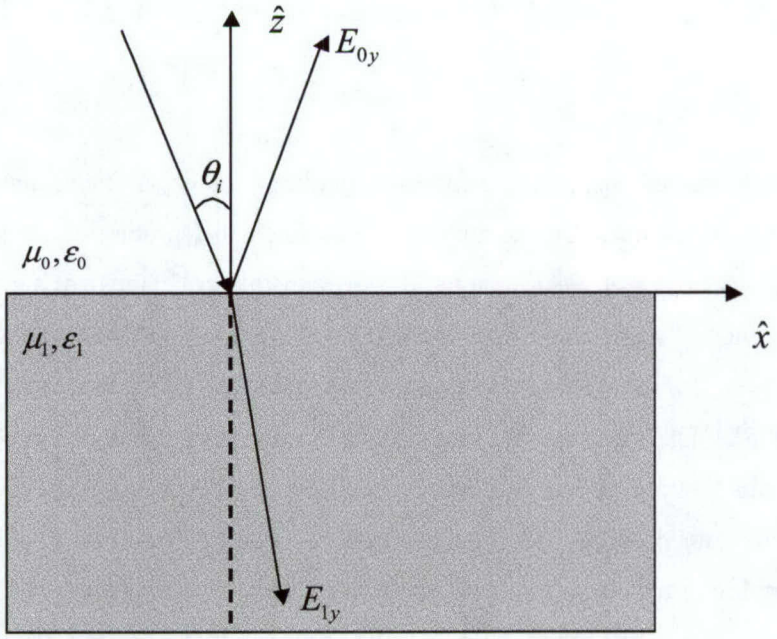

Figure 2.1. An electromagnetic plane wave impinges on a half-space medium with a plane boundary.

The normalized electric field $E_{0y}(x,z,\omega)$ in the upper half-space is composed of the normalized incident and reflected fields, and given as [Kong, 1990]

$$E_{0y}(x,z,\omega) = e^{jk_{0z}z}\, e^{-jk_x x} + R_h(\omega) e^{-jk_{0z}z}\, e^{-jk_x x}, \tag{2.1}$$

where $j = \sqrt{-1}$, $k_{0z} = \sqrt{k_0^2 - k_x^2}$ denotes the z component of the wave vector $\bar{k}_0$ in the upper region, $k_x = k_0 \sin\theta_i$, and $R_h(\omega)$ is the Fresnel reflection coefficient for horizontal polarization, given by

$$R_h(\omega) = \frac{k_{0z} - k_{1z}}{k_{0z} + k_{1z}}. \tag{2.2}$$

Here $k_{1z} = \sqrt{k_1^2 - k_x^2}$ denotes the z component of the wave vector $\bar{k}_1$ in the lower half-space. The normalized transmitted field $E_{1y}(x,z,\omega)$ in the lower region is [Kong, 1990]

$$E_{1y}(x,z,\omega) = T_h(\omega) e^{jk_{1z}z}\, e^{-jk_x x}, \tag{2.3}$$

and $T_h(\omega)$ is the Fresnel transmission coefficient for horizontal polarization, expressed as

$$T_h(\omega) = \frac{2k_{0z}}{k_{0z} + k_{1z}}. \tag{2.4}$$

The formulas for the electric fields inside the media for a vertically polarized incident wave can be found in [Kong, 1990]. It is noted that the wavenumber k_1 depends on the permittivity ε_1 of the lower half-space dispersive medium. The formation of a precursor-like waveform depends on the dispersive behavior of the phase factor $e^{jk_{1z}z}$ in (2.3). Precursors will form only if the medium is strongly dispersive.

2.2 Dielectric Constant Based on Debye Model of Water

The Debye model describes the dielectric response of fluids with permanent dielectric dipole moments. In the frequency domain, the complex relative permittivity of pure water ($\varepsilon = \varepsilon' - j\varepsilon''$) can be described by the following formula [Albanese et al., 1989; Blaschak and Franzen, 1995; Roberts and Peropoulos, 1996]:

$$\varepsilon(f) = \varepsilon_\infty + \frac{\varepsilon_s - \varepsilon_\infty}{1 + j2\pi fT} - j\frac{\sigma}{2\pi f\varepsilon_0}, \tag{2.5}$$

where f is excitation frequency in Hz, and $\varepsilon_0 = 10^{-9}/(36\pi)$ farad/m is the permittivity of free space. The other parameters in (2.5) are generally temperature dependent. At 25°C, their values are [Albanese et al., 1989]: the relaxation time $T = 8.1\times10^{-12}$ sec, the high frequency relative dielectric constant of water $\varepsilon_\infty = 5.5$, and the low frequency relative dielectric constant of water $\varepsilon_s = 78.2$. The relaxation time T gives a dipolar polarization resonance frequency of $f_c = 1/(2\pi T) = 1.96\times10^{10}$ Hz. The conduction loss has been accounted for by the conductivity $\sigma = 10^{-5}$ siemens/m.

The wavenumber in the water medium is complex and can be expressed as $k = k' - jk''$, where k' and k'' are the real and imaginary parts, respectively. The phase delay per unit distance associated with the electromagnetic wave in the dispersive water medium is described by the real part of wavenumber as

$$k' = \frac{2\pi f}{c}\mathrm{Re}\left(\sqrt{\varepsilon(f)}\right), \tag{2.6}$$

where c is the speed of light in vacuum. The attenuation coefficient α is

$$\alpha = k'' = \frac{2\pi f}{c} \mathrm{Im}\left(\sqrt{\varepsilon(f)}\right). \tag{2.7}$$

The field attenuation per unit distance is computed as $\exp(-\alpha)$.

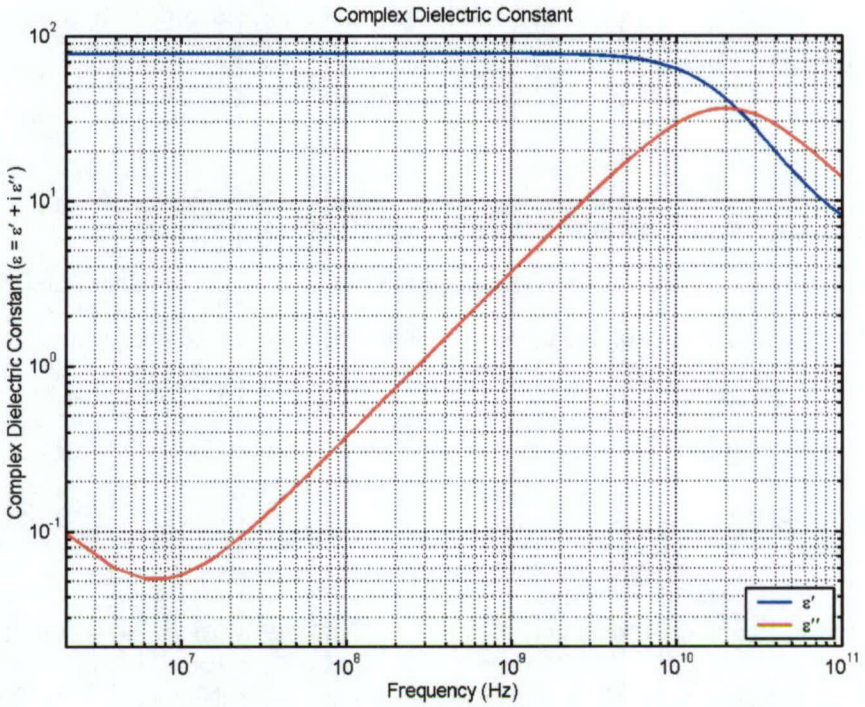

Figure 2.2. The real part, ε', (blue curve) and imaginary part, ε'', (red curve) of the complex dielectric constant of water at $25^{\circ}C$.

Based on (2.5), Figure 2.2 plots the dispersion curves of the real and imaginary parts of the dielectric constant of water at $25^{\circ}C$. From 10 MHz to 10 GHz, the real part of the dielectric constant, ε', varies little with frequency. Over the same range, the imaginary part of the dielectric constant, ε'', increases dramatically with frequency. For frequencies below 10 MHz, the conduction loss term in (2.5) starts to contribute significantly to the imaginary part of the complex dielectric constant of water. It is noted that the roll-off in the real part curve of ε' around the polarization resonance frequency, $f_c = 1.96 \times 10^{10}$ Hz is associated with the peak in the imaginary part curve of ε''.

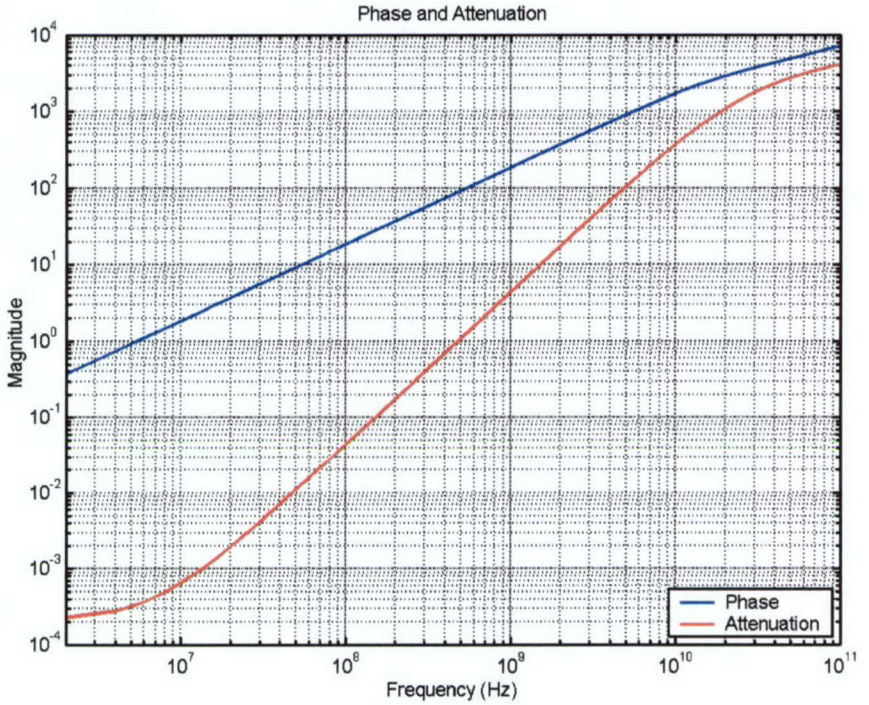

Figure 2.3. Phase (radian/m) dispersion and attenuation coefficient (1/m) for an electromagnetic wave in water medium as a function of frequency.

The magnitude of the phase dispersion, in units of radian/m, and the attenuation coefficient, in units of 1/m, of an electromagnetic wave in a homogeneous water medium are plotted in Figure 2.3 as a function of frequency. Notice that in the frequency range of 10 MHz to 10 GHz, the phase variation increases linearly with frequency while the attenuation coefficient increases approximately as the square of frequency (f^2). The stronger frequency dependence for the attenuation coefficient of electromagnetic waves in a homogeneous, pure water medium shows a distinct difference from the attenuation of electromagnetic waves in an inhomogeneous foliage medium [Mower, 1988; Bessette and Ayasli, 2001]. As will be discussed in later sections, the attenuation of electromagnetic waves in the foliage varies roughly as the first order of frequency.

2.3 Ultra-Wideband Signal Propagation in a Half-Space of Water

The excitation waveform $f(t)$ used in this study is a rectangular pulse modulated simusoid with unit amplitude,

$$f(t)=\begin{cases}\sin[2\pi f_0(t-t_0)] & |t-t_0|\le\dfrac{\tau}{2}\\ 0 & otherwise\end{cases}, \tag{2.8}$$

where f_0 is the carrier frequency, τ is the pulse width, and the pulse is centered at $t=t_0$. This waveform it has the frequency spectrum $F(\omega)$

$$F(\omega)=\left(\frac{j\tau}{2}\right)e^{-j\omega t_0}\left\{\frac{\sin[(\omega+\omega_0)\tau/2]}{(\omega+\omega_0)\tau/2}-\frac{\sin[(\omega-\omega_0)\tau/2]}{(\omega-\omega_0)\tau/2}\right\}, \tag{2.9}$$

where $\omega_0=2\pi f_0$.

From the theory of linear systems [Oppenheim et al., 1997], the response $y(t)$ of a linear time-invariant system, characterized by an impulse response (or Green's function) $h(t)$, to a real input signal $f(t)$ is given by the convolution integral

$$y(t)=\int_{-\infty}^{\infty}dt'\,h(t')\,f(t-t'). \tag{2.10}$$

Taking the Fourier transform of both sides of (2.10) yields the system response in the frequency domain,

$$Y(\omega)=H(\omega)F(\omega), \tag{2.11}$$

where $Y(\omega)$, $H(\omega)$, and $F(\omega)$ represent the Fourier transforms of $y(t)$, $h(t)$, and $f(t)$, respectively, and $H(\omega)$ is the transfer function of the system.

Maxwell's equations are linear and time invariant when they describe propagation in a linear, time invariant medium such as water. Accordingly, the half-space water medium described in Section 2.1 can be treated as a linear system for modeling the propagation and scattering of an ultra-wideband pulse by using linear system theory and Fourier analysis. Thus, the right hand side of equation (2.3) $H_{1\,y}$ (x, z, w), is the medium transfer function for the transmitted signal in the lower half-space. Given the excitation signal spectrum (2.9), the spectrum of the transmitted signal, $Y_t(x,z,\omega)$, at the observation point (x,z) can be expressed as

$$Y_t(x,z,\omega) = H_{1y}(x,z,\omega)F(\omega)\,. \tag{2.12}$$

Similarly, the medium transfer function for the upper half-space is represented by the second term of the right – hand side of equation (2.1). The total signal spectrum , $Y_r(x,z,\omega)$, at the observation point (x,z) in the upper region is

$$Y_r(x,z,\omega) = H_{0y}(x,z,\omega)F(\omega)\,. \tag{2.13}$$

From equations (2.10) and (2.11), it is easily seen that the propagated signal waveform within the water medium in the time domain, $y_t(t,x,z)$, is given by

$$y_t(t,x,z) = F^{-1}\{Y_t(x,z,\omega)\} = F^{-1}\{H_{1y}(x,z,\omega)F(\omega)\}, \tag{2.14}$$

where $F^{-1}\{\ \}$ represents the inverse Fourier transform. Similarly, the total signal waveform in the free space region, $y_r(t,x,z)$, is given by

$$y_r(t,x,z) = F^{-1}\{Y_r(x,z,\omega)\} = F^{-1}\{H_{0y}(x,z,\omega)F(\omega)\}. \tag{2.15}$$

Numerical Fourier transform or Fast Fourier Transform (FFT) techniques can be applied to compute (2.14) and (2.15) [Papoulis, 1987; Oppenheim et al., 1997] to obtain the time domain signal waveforms

Let the incidence angle be $\theta_i = 0^\circ$ (normal incidence), the carrier frequency $f_0 = 1\times10^9\,\text{Hz}$, the pulse width $\tau = 1\times10^{-8}\,\text{sec}$, and the observation point at $x = 0$, and $z = -0.75\,\text{m}$. Figure 2.4 plots the magnitudes of the spectra of the excitation signal (blue curve), the half-space medium transfer function $E_{1y}(x,z,\omega)$ (magenta curve), and the transmitted signal spectrum $Y_t(x,z,\omega)$ (red curve). The peak of the spectrum of the excitation signal is centered at the carrier frequency of 1 GHz. However, this spectrum is not symmetric about the carrier frequency due to the ultra-wide bandwidth of the waveform used. We can see that the magnitude of the half-space medium transfer function decreases rapidly as the frequency increases beyond 1 GHz. This is due to the fact that attenuation increases approximately as the square of frequency. Thus, the half-space medium transfer function behaves like a low-pass filter; the high frequency components in the source spectrum are strongly attenuated and, therefore, absent in the output pulse. The spectrum of the transmitted signal as a function of frequency, calculated from (2.12), is shown as the red curve in Figure 2.4.

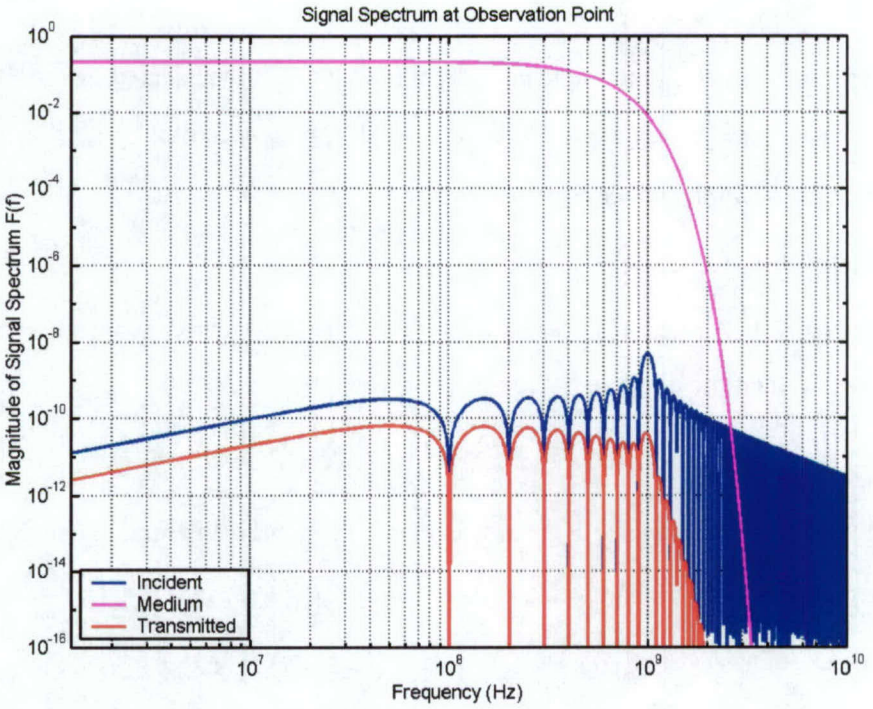

Figure 2.4. The spectra of the excitation signal (blue curve), the half-space medium transfer function $E_{1y}(x,z,\omega)$ (magenta curve), and the transmitted signal $Y_t(x,z,\omega)$ (red curve).

Consider next Figure 2.5. The pulse shape of this applied excitation pulse waveform (green curve), the time evolution of the reflected electric field in the free-space region (blue curve) at the location $(x = 0\,\text{m}, z = 0.75\,\text{m})$, and the time evolution of the propagated electric field within the water medium (red curve) at $(x = 0\,\text{m},\ z = -0.75\,\text{m})$ are shown. The applied excitation is a ten-cycle sine-modulated rectangular pulse of $0.01\,\mu\text{sec}$ duration. The point $t = 0\,\text{sec}$ corresponds to the time when the source pulse is initiated at $z = 0\,\text{m}$. A magnified view of the time evolution of the transmitted and reflected electric fields is also shown in Figure 2.6. The shape of the transmitted signal shows two conspicuous peaks at the leading and trailing edges of the pulse. These are recognized as the precursor-like (Brillouin precursor) waveforms [Albanese et al., 1989; Oughstun, 1991; Oughstun and Sherman, 1995]. The main body of the signal at the carrier frequency is much weaker than the precursor peaks. As can be seen in Figure 2.5, the reflected signal in the free-space region (blue curve) is much stronger than the transmitted signal nor does it show leading and trailing spikes characteristic of precursor waveforms.

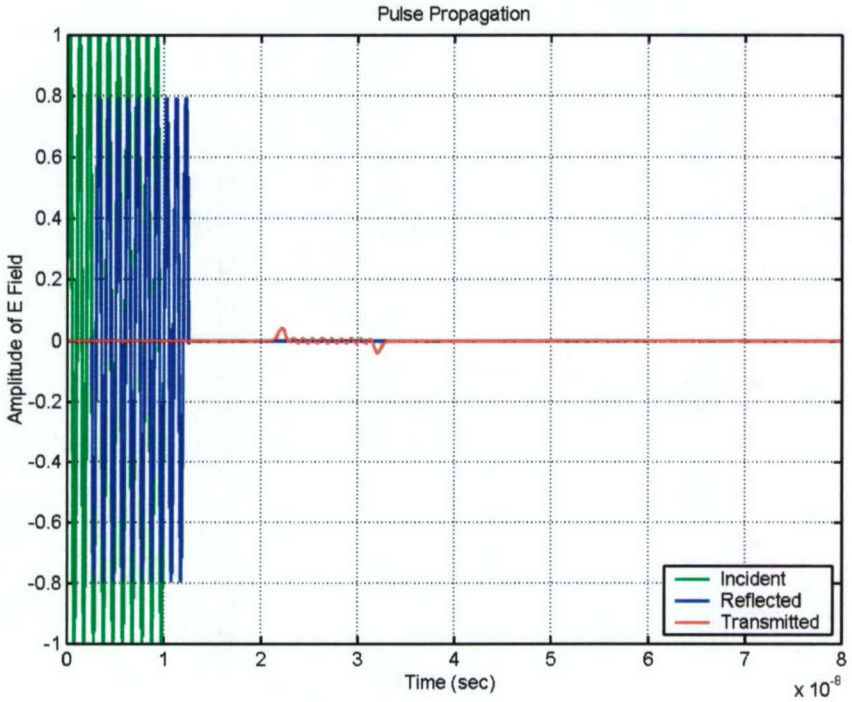

Figure 2.5. The applied excitation pulse (green curve), the time evolution of the reflected electric field in the free-space region (blue curve) at the location $(x = 0\,\mathrm{m},\ z = 0.75\,\mathrm{m})$, and the electric field propagated within the water medium (red curve) at the location $(x = 0\,\mathrm{m},\ z = -0.75\,\mathrm{m})$.

Asymptotic theory is usually applied to analyze the behavior of transient signal propagation in a homogeneous, dispersive medium, in which contour integration techniques in the complex variable domain are employed to perform the complicated integrations [Oughstum, 1991; Oughstun and Sherman; 1995]. That approach can obscure the mechanisms that give rise to precursor-like waveforms. In contrast, the linear systems approach is intuitively simple, rigorous, and transparent to the underlying precursor formation processes.

In fact, the linear systems approach makes the conditions necessary for precursor formation self- evident. That precursors will form can be predicted by inspection from the curves in Figure 2.4. The transfer function of the water medium displays a sharp increase in the attenuation above about 1 GHz. Because of this, the upper sidebands of the incident signal spectrum are severely attenuated and the lower sidebands are equalized. Thus, the spectrum of the signal propagating in the water approximates a boxcar modulated sinusoid in the frequency domain.

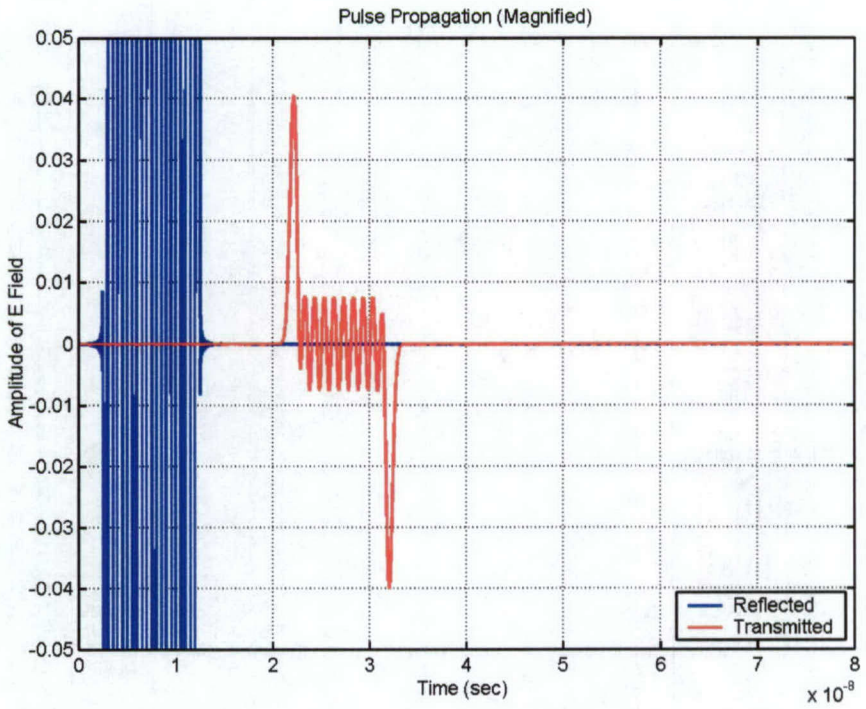

Figure 2.6. A magnified view on the pulse shapes of the reflected electric field in the free-space region (blue curve) at the location $(x = 0\,\mathrm{m}, z = 0.75\,\mathrm{m})$, and the propagated electric field within the water medium (red curve) at the location $(x = 0\,\mathrm{m},\ z = -0.75\,\mathrm{m})$.

The inverse Fourier transform of a boxcar spectrum of frequency is a sinc function of time, and the inverse Fourier transform of a sinusoidal spectrum of frequency results in two similar (δ) functions, one is positive and the other is negative. Thus, the time evolution of transmitted pulse in the water can be thought of as a sinc function of time convolved with a function of time consisting of two (δ) functions, one with positive amplitude and the other with negative. The (δ) functions slide the sinc function along the time axis, which leads to the observation of the precursor-like sinc waveforms at the leading and trailing edges of the waveform as shown in Figure 2.6. If a medium transfer function cannot provide an equalization mechanism for the excitation source spectrum, the medium will not present the precursor distortion effects on the observed time signals. It is also important to notice that the duration of the precursor is inversely proportional to the equalized spectrum bandwidth.

This heuristic argument for the formation of precursors based on linear system analysis is presented to provide qualitative understanding of the conditions necessary to create precursors like responses. However, all of the numerical results presented here result from exact, numerical analysis of the linear system equations.

2.4 Effects of Carrier Frequency and Bandwidth on Attenuation of Ultra-Wideband Signal Propagation

From Figures 2.5 and 2.6, it is clear that the shape of the wave packet is distorted and the electric field is strongly attenuated when the signal propagates through the water medium. The eminent peaks shown in the Brillouin precursor waveform are due to the low frequency components in the spectrum of the excitation pulse. It has been demonstrated [Albanese et al., 1989] that the peak amplitude in the Brillouin precursor in water decreases non-exponentially, which motivates using the Brillouin precursor waveform for FOPEN radar systems. However, radar signal energy, and not signal amplitude, is the important factor for characterizing target detection in the presence of white receiver noise and other sources of interference [Helstrom, 1995]. This will be discussed later. In this section, we will show how the carrier frequency and bandwidth of the excitation signal affect the attenuation of the peak value and energy of the waveform as it propagates through the water.

The excitation signal waveform $f(t)$, as given by (2.8), is a rectangular pulse-modulated sinusoid of unit amplitude. Four different excitation signals are considered: (i) a high carrier frequency at $f_0 = 1\times10^9$ Hz and short pulse duration of $\tau = 1\times10^{-8}$ sec; (ii) a high carrier frequency at $f_0 = 1\times10^9$ Hz and long pulse duration of $\tau = 1\times10^{-7}$ sec; (iii) a low carrier frequency at $f_0 = 2.5\times10^8$ Hz and short pulse duration of $\tau = 1\times10^{-8}$ sec; and (iv) a low carrier frequency at $f_0 = 2.5\times10^8$ Hz and long pulse duration of $\tau = 1\times10^{-7}$ sec. The spectra of these four signals are plotted in Figure 2.7.

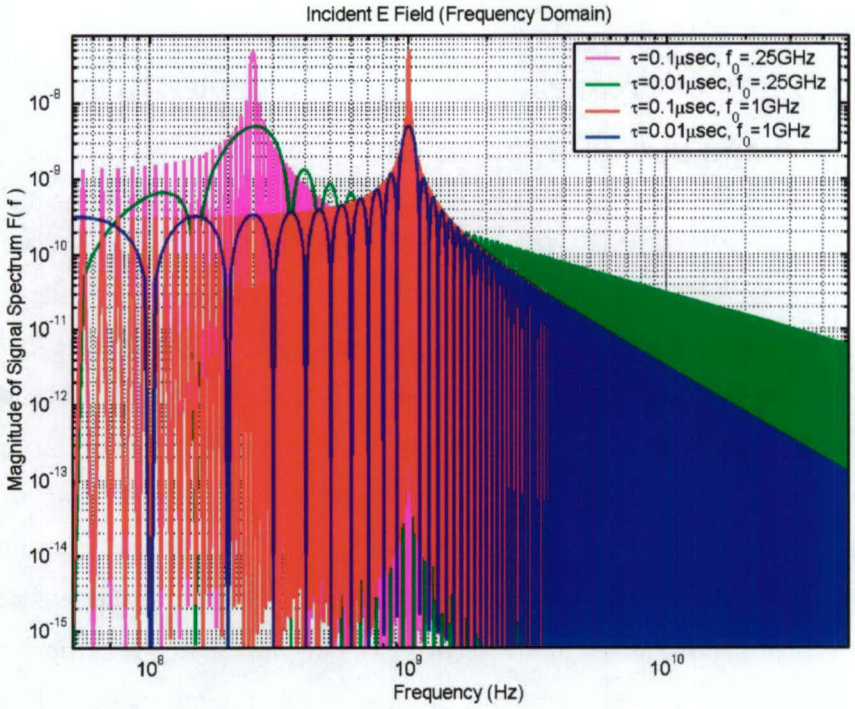

Figure 2.7. The spectra of the excitation signals of unity amplitude as given by (2.8): (i) $f_0 = 1\times10^9$ Hz and $\tau = 1\times10^{-8}$ sec (blue curve); (ii) $f_0 = 1\times10^9$ Hz and $\tau = 1\times10^{-7}$ sec (red curve); (iii) $f_0 = 2.5\times10^8$ Hz and $\tau = 1\times10^{-8}$ sec (green curve); and (iv) $f_0 = 2.5\times10^8$ Hz and $\tau = 1\times10^{-7}$ sec (magenta curve).

In Figure 2.8 we illustrate the attenuation of the electric field peak observed in the water medium as a function of the observation depth for two excitation signals, one with carrier frequency at $f_0 = 1\times10^9$ Hz and pulse duration of $\tau = 1\times10^{-8}$ sec, and the other with carrier frequency at $f_0 = 2.5\times10^8$ Hz and pulse duration of $\tau = 1\times10^{-7}$ sec. For the signal with the higher carrier frequency and the greater frequency bandwidth (shorter pulse duration), the pulse peak amplitude decreases most rapidly at small depths within the water. However, the decrease becomes less rapid at greater depths. The signal with a lower carrier frequency at $f_0 = 2.5\times10^8$ Hz and ten-times narrower bandwidth is attenuated less. For the signal with higher carrier frequency at $f_0 = 1\times10^9$ Hz, the amplitude of pulse's peak at a 1-m depth is approximately 15% of that at the interface.

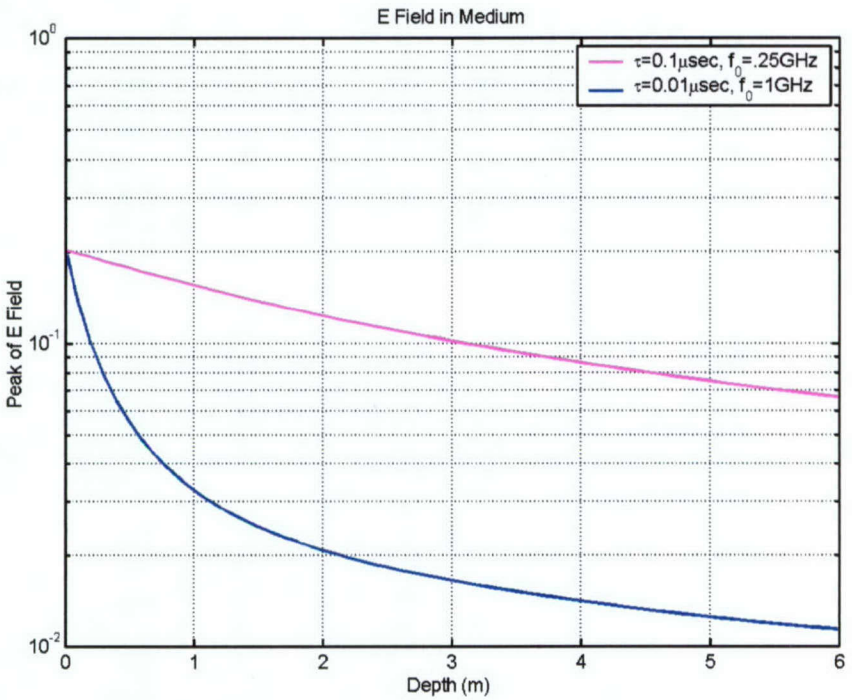

Figure 2.8. The magnitude of the electric field's peak as a function of observation depth in water for two excitation signals: (i) with $f_0 = 1\times10^9$ Hz and $\tau = 1\times10^{-8}$ sec (blue curve), and (ii) with $f_0 = 2.5\times10^8$ Hz and $\tau = 1\times10^{-7}$ sec (magenta curve).

Similarly, in Figure 2.9, we plot the attenuation of the pulse peak within the water medium as a function of distance into the medium in skin depths at the carrier frequency. The skin depth or penetration depth d_p of wave propagation through water is defined as the inverse of attenuation coefficient, $d_p = 1/\alpha$, where α is given by (2.7). With the water dispersive property in (2.5), the skin depth is $d_p = 0.2384$ m for the signal with carrier frequency $f_0 = 1\times10^9$ Hz, and the skin depth is $d_p = 3.656$ m for the signal carrier frequency $f_0 = 2.5\times10^8$ Hz. The water skin depth at the lower carrier frequency is much greater than that at the higher carrier frequency because of the greater attenuation of the higher frequency signal components. It is interesting to note that the two curves shown in Figure 2.9 are almost identical. However, the real penetration depths at four skin depths are 14.58 m and 0.91m for $f_0 = 2.5\times10^8$ Hz and $f_0 = 1\times10^9$ Hz, respectively.

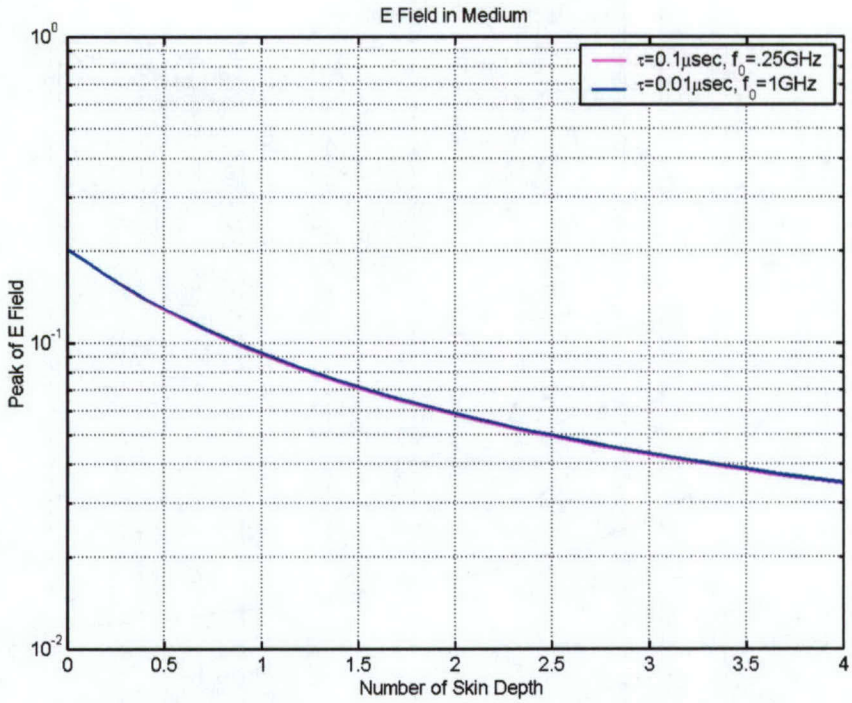

Figure 2.9. The magnitude of the electric field's peak as a function of the number of water skin depths for two excitation signals: (i) with $f_0 = 1\times10^9$ Hz and $\tau = 1\times10^{-8}$ sec (blue curve), and (ii) with $f_0 = 2.5\times10^8$ Hz and $\tau = 1\times10^{-7}$ sec (magenta curve).

To make a reliable detection decision, the radar must receive sufficient target reflected energy in the presence of white noise and other sources of interference. Thus, the energy contained in the reflected target signal is an important design criterion. The total energy associated with a signal $f(t)$ is

$$\int_{-\infty}^{\infty} |f(t)|^2 dt = \int_{-\infty}^{\infty} |F(\omega)|^2 d\omega, \tag{2.16}$$

where the equal sign is due to the Parseval's theorem, and $F(\omega)$ is the frequency spectrum of $f(t)$. Numerical techniques, such as trapezoidal or Simpson's integration method, can be applied to compute the integrals in the time or frequency domain.

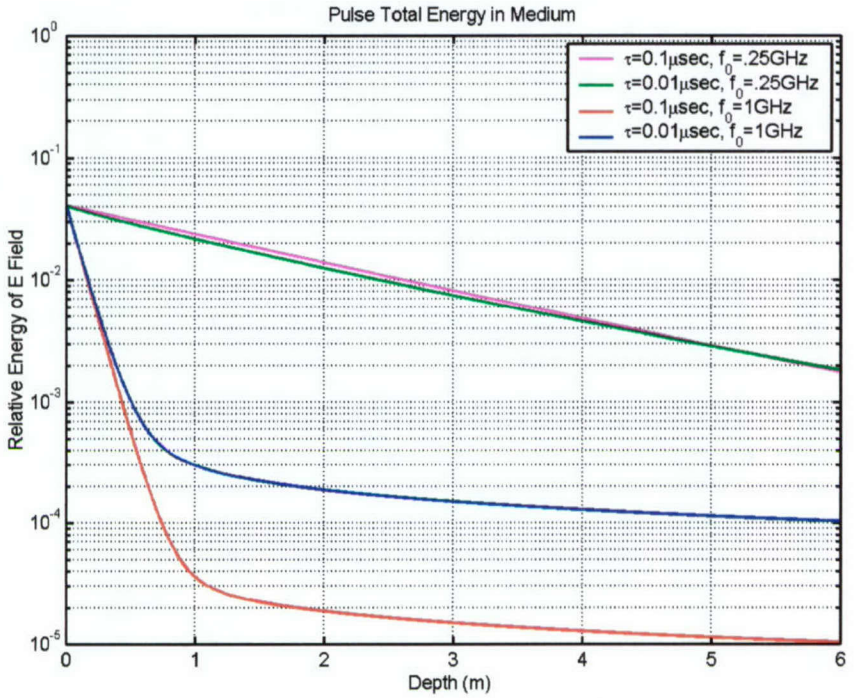

Figure 2.10. The relative total energy of the signal as a function of observation depth in water for four excitation signals: (i) $f_0 = 1\times10^9$ Hz and $\tau = 1\times10^{-8}$ sec (blue curve); (ii) $f_0 = 1\times10^9$ Hz and $\tau = 1\times10^{-7}$ sec (red curve); (iii) $f_0 = 2.5\times10^8$ Hz and $\tau = 1\times10^{-8}$ sec (green curve); and (iv) $f_0 = 2.5\times10^8$ Hz and $\tau = 1\times10^{-7}$ sec (magenta curve).

In Figure 2.10 we plot the relative total energy associated with the electric field in the water as a function of the observation depth for four excitation signals. Their respective carrier frequencies and pulse widths are $f_0 = 1\times10^9$ Hz and $\tau = 1\times10^{-8}$ sec, $f_0 = 1\times10^9$ Hz and $\tau = 1\times10^{-7}$ sec, $f_0 = 2.5\times10^8$ Hz and $\tau = 1\times10^{-8}$ sec, and $f_0 = 2.5\times10^8$ Hz and $\tau = 1\times10^{-7}$ sec. Similarly, the attenuation of pulse energy within the water medium is shown in Figure 2.11 as a function of depth in skin depths. Again, we can see that the total energy contained within the signals having higher carrier frequency $f_0 = 1\times10^9$ Hz decreases exponentially at small depths within the water. Although the higher carrier frequency signal with shorter pulse width (wider frequency bandwidth) shows a slower decrease of total energy than the signal with longer pulse width (narrower frequency bandwidth), the total signal energy at 1m water depth drops to approximately 1% and 0.1% of that at the interface for the higher carrier frequency signals with shorter pulse width ($\tau = 1\times10^{-8}$ sec) and longer pulse width

($\tau = 1\times10^{-7}$ sec), respectively. For the lower carrier frequency at $f_0 = 2.5\times10^8$ Hz, the energy attenuation is about 2/3 at 1m depths. It is clear that the energy penetration into the lossy water for a signal having lower carrier frequency is much superior than the signal with higher carrier frequency. As shown in Figure 2.11, the precursor-like waveform arises, or the associated signal energy attenuation becomes much slower, only after the electric field propagates several skin depths into a lossy and dispersive medium. However, the skin depth of water at lower carrier frequency is much greater than that at the higher carrier frequency.

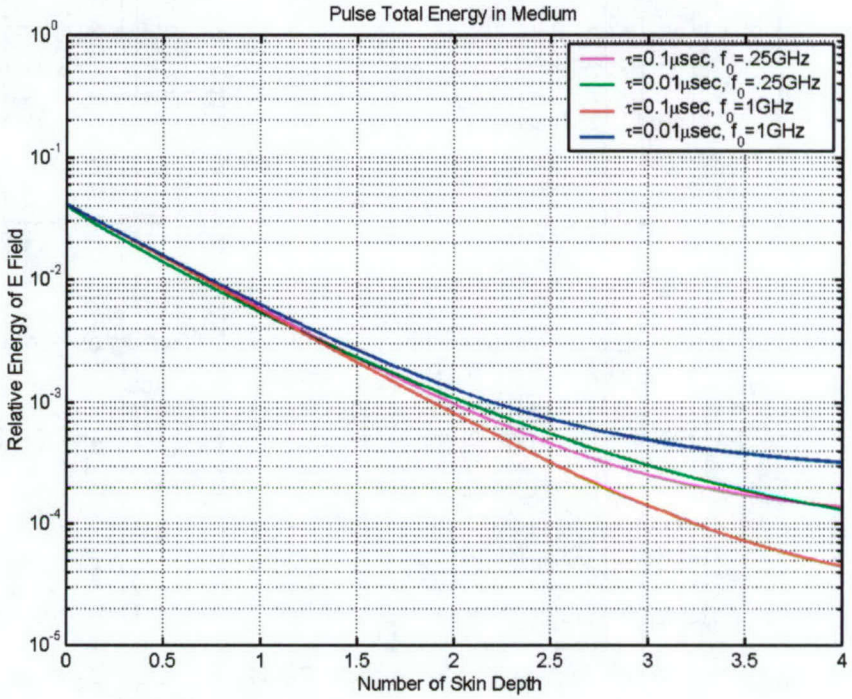

Figure 2.11. The relative total energy of signal as a function of the number of water skin depths for four excitation signals: (i) $f_0 = 1\times10^9$ Hz and $\tau = 1\times10^{-8}$ sec (blue curve); (ii) $f_0 = 1\times10^9$ Hz and $\tau = 1\times10^{-7}$ sec (red curve); (iii) $f_0 = 2.5\times10^8$ Hz and $\tau = 1\times10^{-8}$ *sec* (green curve); and (iv) $f_0 = 2.5\times10^8$ Hz and $\tau = 1\times10^{-7}$ sec (magenta curve).

The numerical results presented in Figures 2.8-2.11 and the medium transfer function shown in Figure 2.4 indicate that propagation requires an excitation signal with a carrier frequency within the pass band of the dispersive and lossy medium to achieve the best penetration. The Brillouin precursor is due to the low frequency components of the excitation pulse that are in the water medium pass band.

2.5 Ultra-Wideband Signal Propagation through a Slab of Water

The half-space homogeneous medium model described in Section 2.1 can be extended to a slab model, which more closely resembles a foliage layer. Figure 2.12 shows a horizontally polarized, TE electromagnetic plane wave impinging on a slab of dielectric medium, where θ_i is the incidence angle and d is the slab thickness. The boundary interfaces are at $z=0$ and $z=-d$. The upper half-space is air characterized by the wavenumber $k_0=\omega\sqrt{\mu_0\varepsilon_0}$, with μ_0 and ε_0 being the respective permeability and permittivity of free-space. The lower half-space is a homogeneous dielectric medium that is characterized by the wavenumber $k_2=\omega\sqrt{\mu_2\,\varepsilon_2}$, where μ_2 and ε_2 are the respective permeability and permittivity. The slab is filled with a dielectric material, which is characterized by the wavenumber $k_1=\omega\sqrt{\mu_1\,\varepsilon_1}$ and μ_1 and ε_1 are the respective permeability and permittivity.

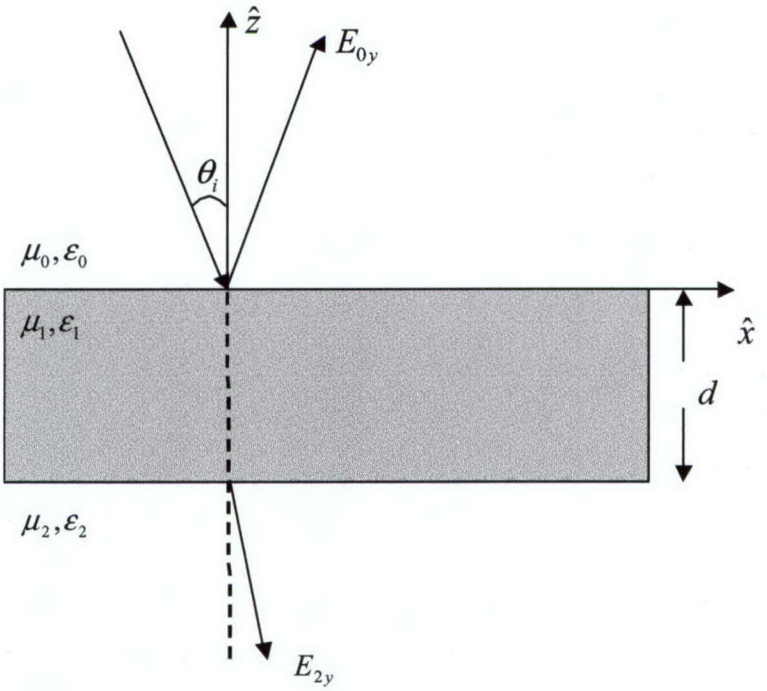

Figure 2.12. An electromagnetic plane wave of incidence angle θ_i impinges on a slab medium of thickness d with plane boundaries.

We assume that $\mu_2 = \mu_1 = \mu_0$ is independent of frequency, while $\varepsilon_1 = \varepsilon_1(\omega)$ and $\varepsilon_2 = \varepsilon_2(\omega)$ are functions of frequency.

The normalized electric field in the upper half-space, $E_{0y}(x,z,\omega)$, is composed of the incident and reflected fields and is given as [Kong, 1990]

$$E_{0y}(x,z,\omega) = e^{jk_{0z}z}\, e^{-jk_x x} + R_h(\omega) e^{-jk_{0z}z}\, e^{-jk_x x}, \tag{2.17}$$

where $R_h(\omega)$ is the Fresnel reflection coefficient for the horizontal polarization,

$$R_h(\omega) = \frac{R_{01}(\omega) + R_{12}(\omega) e^{-j2k_{1z}d}}{1 + R_{01}(\omega) R_{12}(\omega) e^{-j2k_{1z}d}}. \tag{2.18}$$

Here $R_{i(i+1)}(\omega)$ denote the reflection coefficient for waves in the region i that is due to the boundary separating regions i and $i+1$. $R_{01}(\omega)$ and $R_{12}(\omega)$ are given as

$$R_{01}(\omega) = \frac{k_{0z} - k_{1z}}{k_{0z} + k_{1z}}, \tag{2.19}$$

$$R_{12}(\omega) = \frac{k_{1z} - k_{2z}}{k_{1z} + k_{2z}}. \tag{2.20}$$

Here $k_{2z} = \sqrt{k_2^2 - k_x^2}$ denotes the z component of the wave vector $\bar{k}_2$ in the lower half-space. The normalized transmitted field $E_{2y}(x,z,\omega)$ in the lower half-space is [Kong, 1990]

$$E_{2y}(x,z,\omega) = T_h(\omega) e^{jk_{2z}z}\, e^{-jk_x x}, \tag{2.21}$$

and $T_h(\omega)$ is the Fresnel transmission coefficient for horizontal polarization

$$T_h(\omega) = \frac{4 e^{-j(k_{1z} - k_{2z})d}}{\left(1 + \frac{k_{1z}}{k_{0z}}\right)\left(1 + \frac{k_{2z}}{k_{1z}}\right)\left(1 + R_{01}(\omega) R_{12}(\omega) e^{-j2k_{1z}d}\right)}. \tag{2.22}$$

The formulas for various electric fields inside media can be found in [Kong, 1990] for vertically polarized incident originals. For a medium with a non-dispersive lower half-space and a dispersive slab material, the wavenumber k_2 becomes a constant, independent of frequency,

while the wavenumber $k_1(\omega)$ is a function of frequency. This frequency dependence admits to the formation of precursor-like waveforms since wave propagation depends on the behavior of the factor $e^{jk_{1z}d}$ shown in both (2.18) and (2.22).

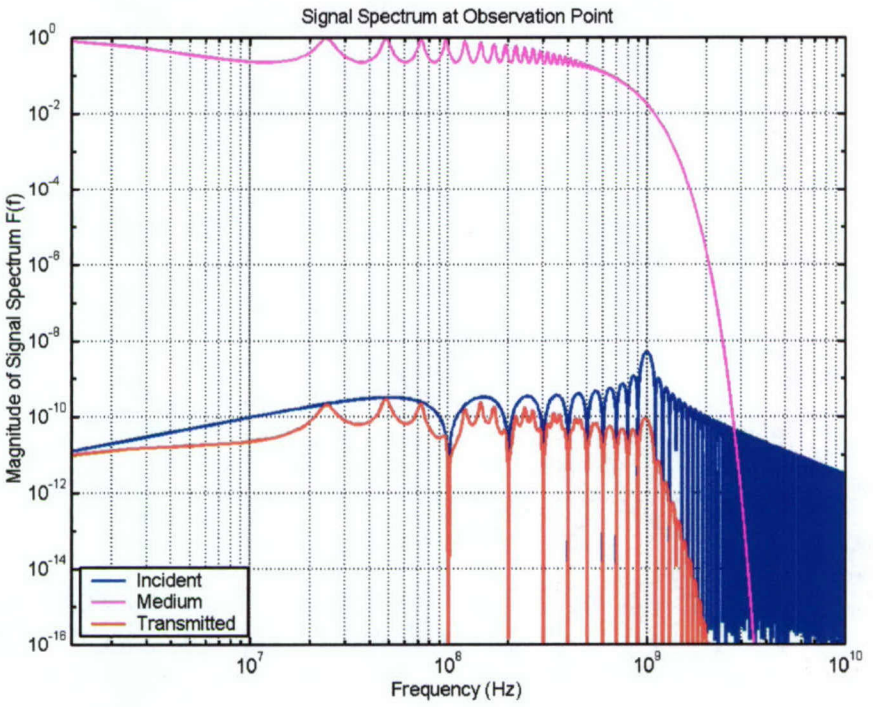

Figure 2.13. The spectra of the excitation signal (blue curve), the slab medium transfer function $E_{1y}(x,z,\omega)$ (magenta curve), and the transmitted signal $Y_t(x,z,\omega)$ (red curve).

We consider a normal incidence of the pulse given by (2.8), with the carrier frequency $f_0 = 1\times10^9\,Hz$ and pulse width $\tau = 1\times10^{-8}\,sec$, upon a water slab of width $d = 0.7\,m$. The lower half-space is assumed to be free-space. The observation point is set at $x = 0$, and $z = -0.75\,m$, just beyond the second boundary. Figure 2.13 plots the magnitudes for the spectra of the excitation signal (blue curve), the slab medium transfer function $E_{2y}(x,z,\omega)$ (magenta curve), and the transmitted signal spectrum (red curve). In a manner similar to Figure 2.4, the magnitude of the slab medium transfer function decreases rapidly with frequency above 1 GHz. The oscillations in the spectrum of the slab medium transfer function over the lower frequency portion are caused by the interference between the up-going and down-going waves within the

slab. The effects of multiple scattering interactions between two boundaries are also shown in the spectrum of the transmitted signal.

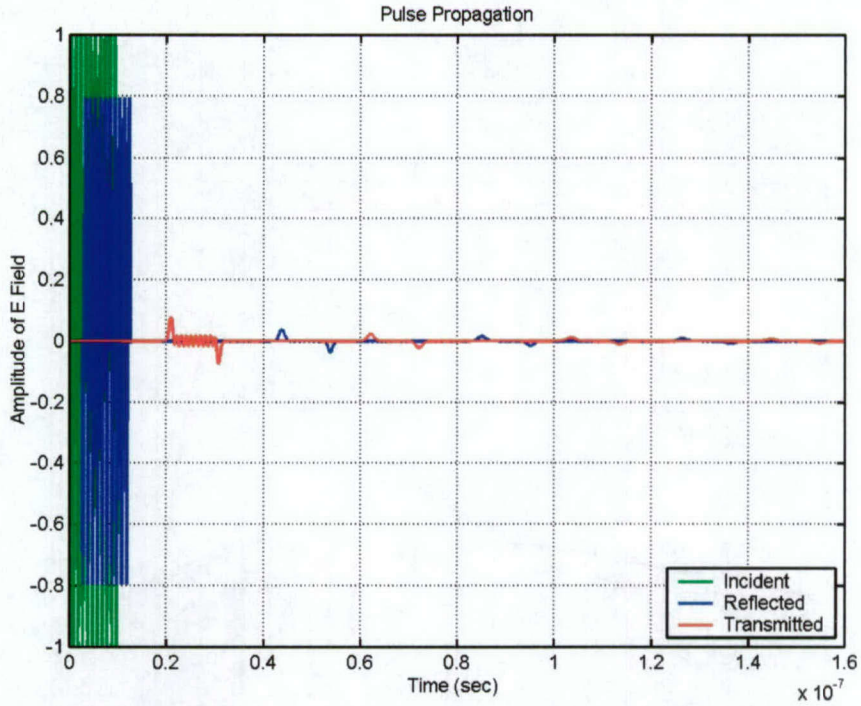

Figure 2.14. The pulse shape of the applied excitation signal (green curve), the time evolutions of the reflected electric field in the free-space region (blue curve) at the location $(x = 0\,\text{m},\ z = 0.75\,\text{m})$, and the propagated electric field through the water slab (red curve) at the location $(x = 0\,\text{m},\ z = -0.75\,\text{m})$.

Figure 2.14 shows the pulse shape of this applied excitation pulse waveform (green curve), the time evolution of the reflected electric field in the free-space region (blue curve) at the location $(x = 0\,\text{m}, z = 0.75\,\text{m})$, and the time evolution of the propagated electric field through the water slab (red curve) at the location $(x = 0\,\text{m},\ z = -0.75\,\text{m})$. The applied excitation is a ten-cycle sine-modulated rectangular pulse of $0.01\mu\text{sec}$ duration. The point $t = 0$ corresponds to the time when the leading edge of the source pulse reaches $z = 0$. A magnified view on the time evolution of the transmitted and reflected electric fields is also shown in Figure 2.15. It is interesting to note that both transmitted and reflected fields have the precursor-like waveforms, which is different from the half-space water medium case in Section 2.3. Due to the multiple interactions between the two boundaries of water slab, a succession of multiple precursors, having similar shapes but with attenuated peak amplitudes, are observed at later times.

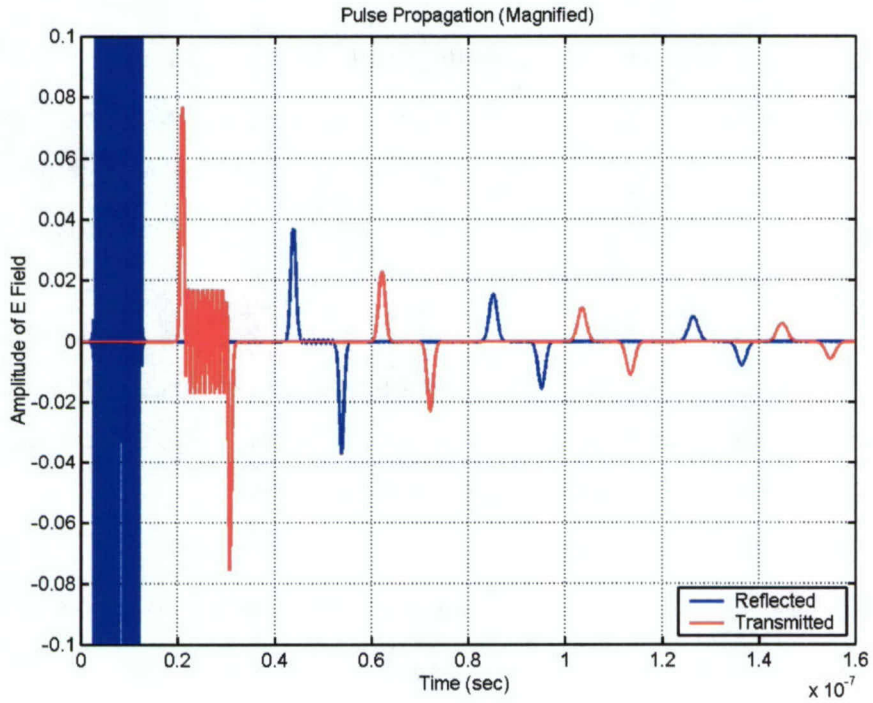

Figure 2.15. A magnified view on the pulse shapes of the reflected electric field in the free-space region (blue curve) at the location $(x = 0\,\text{m},\, z = 0.75\,\text{m})$, and the propagated electric field through the water slab (red curve) at the location $(x = 0\,\text{m},\ z = -0.75\,\text{m})$.

2.6 Step Response of a Water Half Space

To this point, we have considered the response of a half space and slab of Debye medium excited by an electromagnetic wave with a rectangular pulse modulated carrier. Now, we extend this analysis to determine the response at varying depths into a half space of water medium due to a wave with a step modulated carrier and assess the conditions for precursor excitation due to the step modulation.

Consider a half space of water characterized electrically as a Debye medium with complex dielectric constant as described in Section 2.2. The medium is excited with a plane wave perpendicular to the free space/medium interface. The temporal variation of the plane wave is given as a step modulated, exponentially decaying sinusoid given by

$$E(t) = \begin{cases} E_0\, e^{-\alpha t} \sin(\omega t + \phi) & \textit{for } t \geq 0 \\ 0 & \textit{otherwise} \end{cases} \tag{2.23}$$

In this analysis, the carrier frequency $\omega/2\pi = 2.5GHz$ and the exponential time constant $1/\alpha = 1n\sec$. We perform the analysis with $\phi = 0$ (sinusoidal carrier with no field discontinuity) and $\pi/2$ (cosinusoidal carrier with step discontinuity at t=0). The response to a plane wave with arbitrary phase can be determined from the superposition of the responses due to these two phase conditions. The signal amplitude E_0 is chosen so that the signal has the same (unit) energy for both cases analyzed.

Figure 2.16 shows the distribution of signal power with frequency for the excitation signals and the response signals at 0.1, 1 and 10 meters into the Debye half space. Consider first the spectrum of the excitation, shown in the dotted curves, for the sinusoidal and cosinusoidal excitations. Both spectra show the concentration of energy about the carrier frequency of 2.5 GHz. The spectrum of the signal with the sinusoidal carrier (no signal discontinuity at $t = 0$) has a frequency dependence of $1/(f - f_c)^2$ for frequencies above the carrier frequency f_c while the spectrum of the signal with cosinusoidal carrier (signal discontinuity at $t = 0$) has a frequency dependence of $1/(f - f_c)$. Since both signals have the same energy, the areas bounded by their spectra are the same with the consequence that the low frequency spectral level of the sinusoidal carrier signal exceeds the spectral level of the cosinusoidal carrier signal. As we have seen, the formation of precursors in the medium is dependent on the residual low frequency spectrum after medium attenuation. Thus, we would expect that the sinusoidal carrier signal with no waveform discontinuity at $t = 0$ and greater low frequency spectral content would yield greater precursor-like effects.

The spectra of the response signals at 0.1, 1, and 10 meters into the Debye medium are shown in Figure 2.16 also. At the smallest depth, 0.1 meter, both signals contain small residual carrier frequency effects. However, at greater depths, 1 meter and 10 meters, the medium attenuation has eliminated any residual carrier frequency content within the power density levels plotted. In fact, at 1 and 10 meters, the spectrum is uniform until the "Gaussian-like" frequency dependency of the medium attenuation provides a high frequency cut off. The only exception is a slight high frequency peaking of the cosinusoidal signal at 1 meter depth.

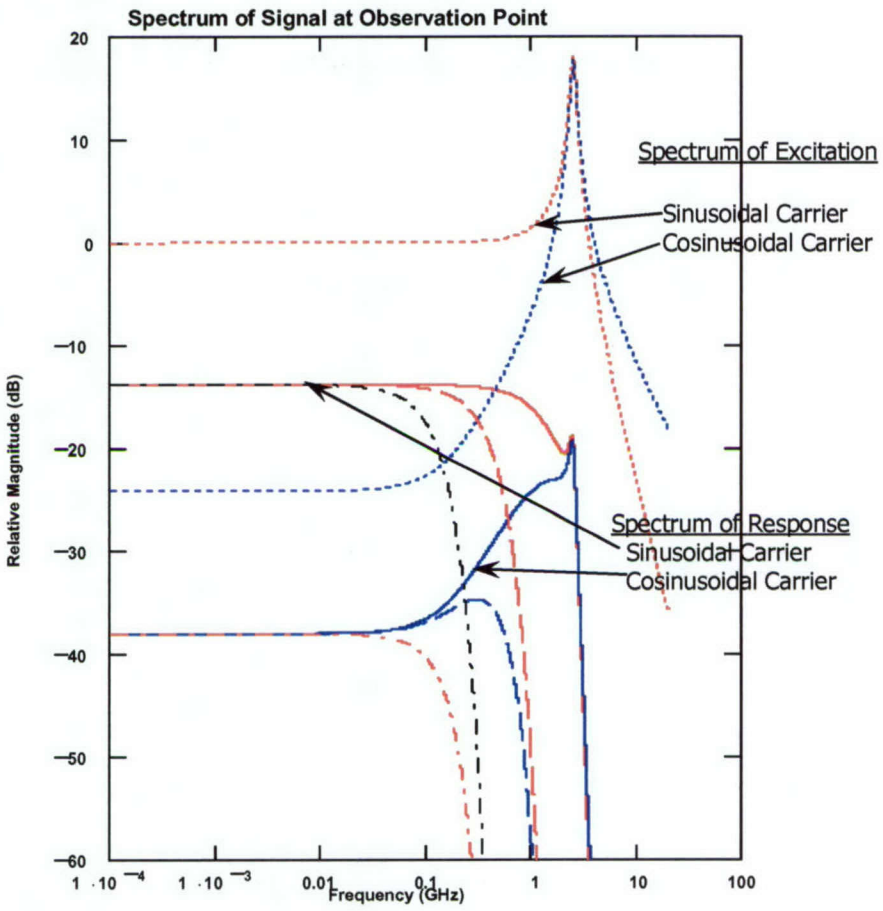

Figure 2.16. The frequency response of the excitation signal (sinusoidal and cosinusoidal carriers) and the corresponding reponse at 0.1, 1 and 10 meters into the slab of Debye medium.

Figure 2.17 shows the corresponding temporal response of the Debye medium to sinusoidal and cosinusoidal step excitation signals at 0.1, 1 and 10 meter depths. These temporal responses show evidence of "precursor-like" behavior. At 0.1 meter depth, the signals are larger and the carrier frequency dominates the response. At greater depths, the responses are delayed and greatly attenuated. The responses exhibit video-pulse-like behavior dictated by the residual bandwidth determined by the medium attenuation and the uniform, low frequency content of the excitation signal. Note that the duration of the responses at 10 m are approximately three times those at 1 m. Also, the amplitudes of the responses with sinusoidal excitation are much larger than those of the cosinusoidal excitation due to the greater low frequency spectrum of the former excitation (Figure 2.16). The response due to cosinusoidal excitation at 1 meter exhibits a residual sinusoidal behavior due to the spectral peaking that was observed in Figure 2.16.

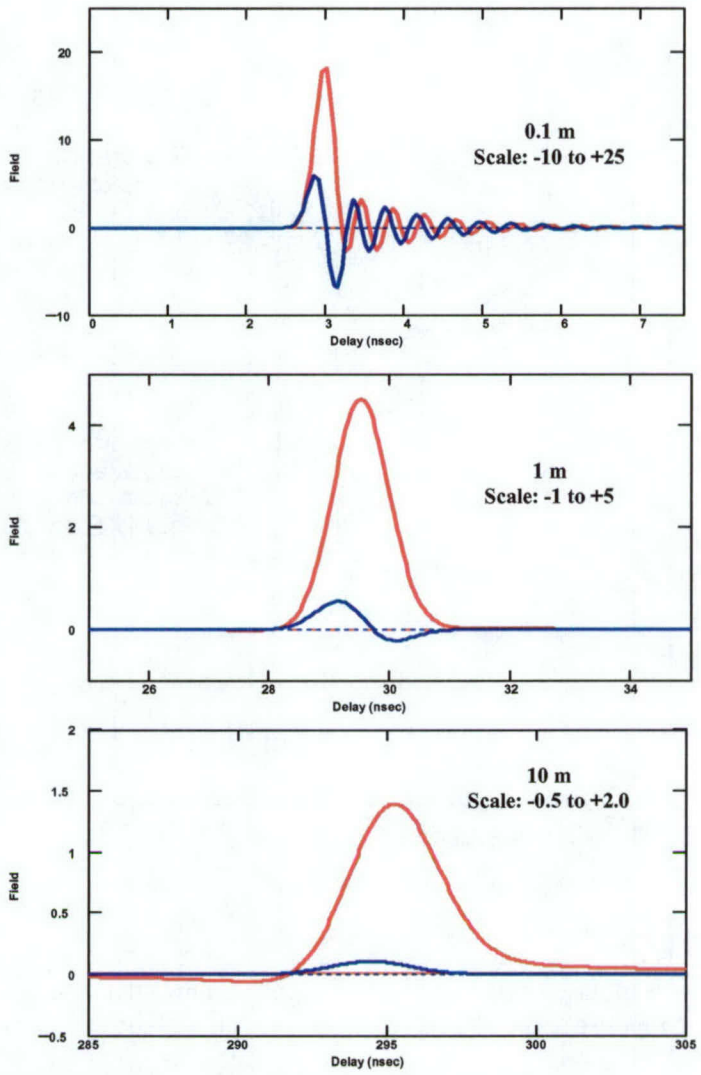

Figure 2.17. Temporal response of a Debye medium half space to a unit energy, exponentially decaying step function with sinusoidal and cosinusoidal carrier. Note differing abscissa and ordinate scales. Larger responses are due to the sinusoidal carrier signal.

This example illustrates further the importance of the low frequency content of the excitation signal in producing "precursor-like" behavior in the response due to a Debye medium. It is the low frequency content that survives medium attenuation and thus it is important that the excitation signal spectrum be rich in these surviving frequency components. However, low frequency signals are often more difficult to radiate and receive due to limited aperture antennas. Also, discrete target reflectivity is limited at lower frequencies due to Rayleigh scattering effects and target-ground interaction producing multipath cancellation. Thus, a more realistic assessment of ultra-wideband phenomenology for radar applications should include a more realistic

assessment of the importance of low frequency limitations on the formation of "precursor-like" responses. This will be discussed in the next section.

3. Scattering by a Target Embedded in a Half-Space Dispersive Water Medium

In this section we extend the preceding analysis of the propagation of an electromagnetic wave in water to include the reflection from a perfectly conducting sphere embedded in the water medium, as illustrated in Figure 3.1. A uniform plane wave is assumed to be normally incident on the water surface. A perfectly conducting sphere is located at varying depths from the interface in a medium with free space permeability and conductivity and complex Debye permittivity as characterized in previous sections. The sphere diameter is chosen to be 4 mm so that the sphere is resonant for the wavelength of the carrier frequency in the medium with a low frequency dielectric constant of approximately 80.

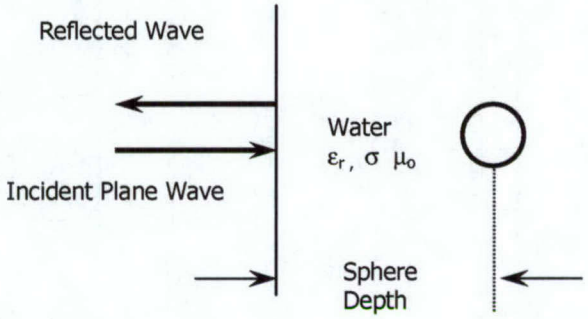

Figure 3.1. A plane electromagnetic wave is incident on a perfect conducting spherical target embedded in a half-space dispersive water medium, which is characterized by the relative complex permittivity ε_r, conductivity σ, and permeability μ_0.

The analysis we provide is approximate. The scattering from the perfectly conducing sphere is characterized by the Mie series solution to Maxwell's equations [Balanis, 1989] where it is assumed that the medium surrounding the sphere is lossless and homogeneous. Thus, in using the Mie series, we neglect any attenuation of the incident wave due to the medium as the wave transverses the sphere. This is an acceptable assumption since the sphere diameter is a small fraction of the medium skin depth at the carrier frequency assumed to be 2.5 GHz. We further neglect distortion of the sphere surface currents due to currents induced in the surrounding medium.

The inhomogeneity of the medium surrounding the sphere, which is neglected in the Mie series solution, is included approximately as follows. The sphere depth is chosen such that the interface between the medium and free space is in the far field of the sphere. Thus, the scattered field from the sphere behaves locally as a plane wave at the interface and the scattered field is both transmitted and reflected by the interface according to the laws of geometrical optics. In this analysis, we consider only the transmission of the scattered field at the interface and neglect any reflected fields from the interface that interact with the sphere causing late time reverberation between the interface and the sphere.

This scattering analysis is included to evaluate the physical effects of low frequency signal attenuation on the formation of Brillouin precursors by propagation and object scattering in a dispersive medium. Any remote sensing or radar application of precursor propagation will encounter the natural loss of low frequency energy in the received signal due to a number of unavoidable physical mechanisms. Any radiating antenna of fixed size used for transmission and reception of electromagnetic energy will exhibit reduced gain at low frequencies when the wavelength is large in comparison with the antenna size. Similarly, scattering of volumetric targets decreases with frequency according to Rayleigh scattering laws when the target is small compared to wavelength. When the target is located adjacent to a ground plane and viewed at small depression angles, target-surface multipath further reduces scatter at low frequencies. Thus, in the analysis provided here, the low frequency Rayleigh scattering from the embedded sphere is included via the Mie series and is a proxy for typical low frequency limitations on precursor formation for radar applications.

3.1 Analysis

With the assumptions and approximations discussed above, the complex transmission from the incident plane wave to the scattered wave at the interface can be expressed as the product of individual transmission coefficients at each radian frequency, $\omega = 2\pi f$,

$$T(\omega) = T_{am}(\omega)\, T_{ma}(\omega)\, T_s(\omega)\, e^{-j2k(\omega)r_s}, \tag{3.1}$$

where $T_{am}(\omega)$ is the transmission coefficient from air to medium,

$$T_{am}(\omega) = \frac{2\,\eta(\omega)}{1+\eta(\omega)}, \tag{3.2}$$

$T_{ma}(\omega)$ is the transmission coefficient from medium to air,

$$T_{ma}(\omega) = \frac{2}{1+\eta(\omega)}. \tag{3.3}$$

$T_s(\omega)$ is the field scattering coefficient for the sphere from the Mie series [Balanis, 1989], r_s is the depth of the sphere center inside the water medium, $k(\omega)$ is the complex wavenumber of the medium, $k(\omega) = \frac{\omega}{c}\sqrt{\varepsilon_r(\omega)}$, and

$$\eta(\omega) = \sqrt{\frac{1}{\varepsilon_r(\omega)}}. \tag{3.4}$$

In the expression (3.1), we have neglected the $1/r_s$ decrease in the signal scattered from the sphere due to scattered field spatial divergence.

Because of the linearity of Maxwell's equations and the medium, the Fourier transform of the plane wave reflected from the sphere/medium at the medium interface is given by

$$F_r(j\omega) = T(\omega) F_i(j\omega) \tag{3.5}$$

where $F_i(j\omega)$ is the Fourier transform of the incident waveform, and $F_r(j\omega)$ is the Fourier transform of the reflected waveform at the interface.

The temporal response of the scattered signal can be calculated from the inverse Fourier transform of $F_r(j\omega)$ numerically or analytically. The next section describes the scattered signal response in the frequency and time domains from this analysis.

3.2 Scattered Field Response

Figure 3.2 shows this power transfer function, $|T(\omega)|^2$, the power spectrum of the reflected signal, $|F_r(j\omega)|^2$, and the sphere relative radar cross section as a function of frequency, f, for the sphere located at 5 mm, 80 mm and 255 mm from the interface. These sphere depths correspond to 0.16, 2.7, and 8.5 skin depths, respectively, at the carrier frequency of the signal, 2.5 GHz. The medium is water with dispersive properties defined earlier in Section 2.2. The duration of the excitation pulse is 2.4 nsec and so the pulse contains 6 cycles of the carrier signal.

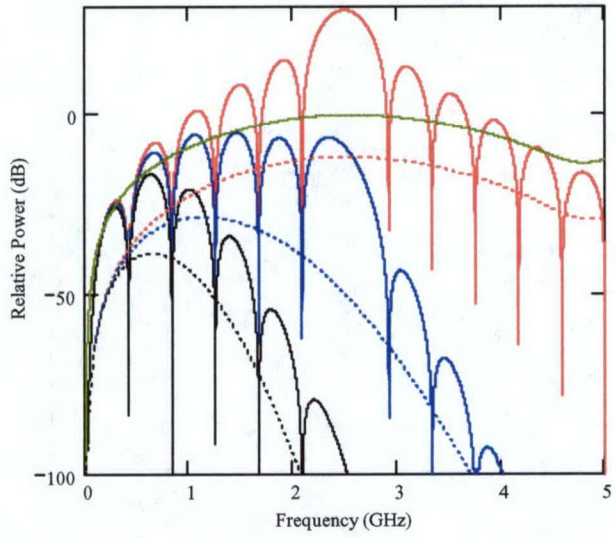

Figure 3.2. The power transfer function, $|T(\omega)|^2$ (green), the power spectrum of the reflected signal, $|F_r(j\omega)|^2$ (solid curve), and the sphere relative radar cross section are shown as a function of frequency for the sphere located at 5 mm (red), 80 mm (blue) and 255 mm (black) from the interface (dashed curve).

When the sphere is near the interface, the power transfer function is shaped principally by the sphere radar cross section with little evidence of high frequency attenuation due to the medium. Thus, the spectrum of the scattered signal is that which might be expected from the sphere in free space, attenuated by the medium. At a depth of 80 mm (2.7 skin depths), the spectrum of the scattered signal shows substantial attenuation at frequencies above the carrier frequency of 2.5 GHz as well as the low frequency Rayleigh attenuation due to the sphere scattering. The signal spectrum is equalized over the band from 500 MHz to 2.5 GHz. Finally, at the greatest depth of 255 mm (8.5 skin depths), the signal is significantly bandwidth limited to the lower sidebands of the excitation by the Rayleigh scattering and the medium attenuation.

Figure 3.3 shows the time response of the scattered signal found from the numerical inverse Fourier transform of $F_r(j\omega)$, using the discrete Fourier transform. Note that the pulse envelope scale is logarithmic (dB). The envelope of the scattered signal (without the carrier frequency) exhibits precursor-like behavior only when the sphere is located several skin depths in the medium. The precursors occur at the leading and trailing edges of the response waveform due to the sinusoidal modulation imposed on the signal spectrum by the incident pulse. The duration of the precursors increase with increasing sphere depth due to the high frequency bandwidth limitations of the response signal imposed by the medium attenuation. Note also that the signal is

greatly attenuated (~ 50dB at 8.5 skin depths) due to the medium loss when compared to the response when the sphere is near the surface.

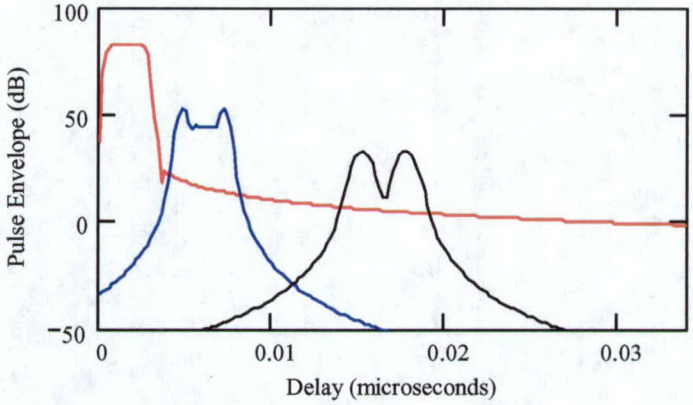

Figure 3.3. Time responses of reflected signals from a sphere embedded in a half-space of water. The sphere is located at 3 different skin depths, 0.16 (red curve), 2.7 (blue curve), and 8.5 (black curve).

We conclude that precursors occur in the radar scattering process due to the dispersive nature of the medium surrounding the scattering object. The low frequency attenuation of the excitation signal due to Rayleigh scattering limits the bandwidth over which received signal power is equalized and thus increases the duration of the precursors and decreases the energy contained in the precursors. Other sources of low frequency attenuation of the excitation, such as those imposed by the transmit-receive antenna gain and target-ground multipath, are likely to cause the same qualitative effects.

3.3 Radar Performance Measures and Transmit Waveform Selection

Airborne or spaceborne radars for the detection of ground targets must be designed with two performance goals in mind. First, the radar must receive sufficient target energy to insure detection in the presence of receiver noise and other sources of interference. Second, the transmitted waveform, transmit-receive antenna patterns and receive signal processing must reject ground reflections sufficiently to enable target detection via distinguishing target properties such as relative motion with respect to the ground. Thus, a necessary condition for target detection with air or spaceborne radars is sufficient target signal to noise to provide reliable detection. When the interfering noise is white or spectrally constant over the bandwidth of the excitation signal, the signal to noise is conveniently expressed as the ratio of receive signal energy to the

noise power spectral density. In order to use this observation and to select the best radar interrogation waveform to excite a target embedded in a dispersive medium, we model the radar system along with its dispersive propagation and scattering mechanisms as a linear system with matched filter processing, as illustrated in Figure 3.4. In this model, pertinent features of the radar are cascaded linear systems with complex transfer functions representing two way propagation in the dispersive medium surrounding a target and target scattering. These cascaded linear systems are excited by the radar transmitted waveform, $s_i(t)$, giving a response $s_r(t)$ at the radar receiver. The total signal at the receiver is the superposition of $s_r(t)$ and additive white noise with constant power spectral density.

The results of classical detection theory [Helstrom, 1995] declare that the linear receiver that maximizes the probability of detection of the signal $s_r(t)$ with constant probability of false detections due to the white noise is a filter matched to the signal. Thus the filter is matched to distortions in the incident waveform due to the dispersion of the medium and target. The output of the matched filter is sampled at the instant of time when the filter output due to the signal is a maximum. This sampled output is the statistic used to declare signal present or absent. The probability of detection is a monotonic function of the signal to noise of this statistic, which, in turn, is proportional to the total energy in the received signal, $s_r(t)$.

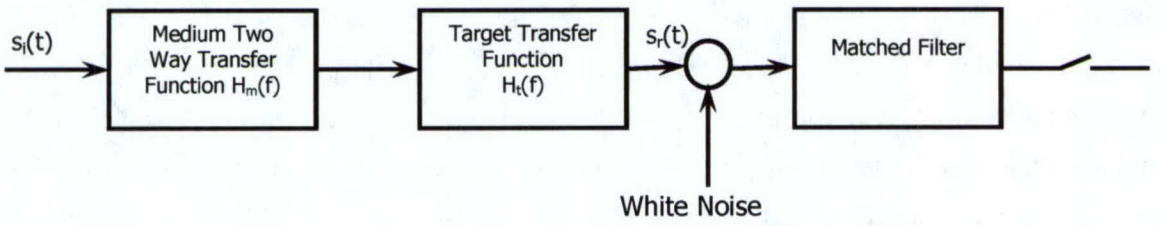

Figure 3.4. Block diagram for modeling the radar system with its dispersive propagation and scattering mechanisms as a linear system with matched filter processing.

It follows then that to maximize the detection of a known target embedded in a dispersive medium with known properties and with constant probability of false alarm due to additive white noise, the radar excitation signal $s_i(t)$ should be selected to maximize the following expression

$$\int_{-\infty}^{\infty} |H_m(f)|^2 \, |H_t(f)|^2 \, |S_i(f)|^2 \, df \,, \tag{3.6}$$

subject to the constraint that the total energy in the excitation waveform is a constant, that is

$$\int_{-\infty}^{\infty} |S_i(f)|^2 \, df = constant \,. \tag{3.7}$$

In these expressions, $H_m(f)$ is the medium two-way transfer function. $H_t(f)$ is the target transfer function, and $S_i(f)$ is the Fourier transform of the excitation signal $s_i(t)$.

The solution to this constrained maximization problem is clear. Since $|H_m(f)|^2$ and $|H_t(f)|^2$ represent the assumed known power transfer functions of the medium and the target, respectively, they are non-negative functions of frequency. Thus, to maximize the energy in the detection statistic, the excitation signal should have its power spectral density, $|S_i(f)|^2$ concentrated at a frequency f_0 where the power transfer function $|H_m(f)|^2 |H_t(f)|^2$ is a maximum. Thus, the signal that maximizes the detection probability is concentrated at f_0 over a bandwidth which is narrow compared to the bandwidth of $|H_m(f)|^2 |H_t(f)|^2$ and which is dictated realistically by other considerations such as limitations on the radar waveform duty cycle and resolution/clutter suppression requirements.

Figure 3.5 illustrates the consequences of this analysis. In this figure, we compare three signal excitations of a sphere embedded in water with dispersion described by the Debye model with parameters as defined earlier in this report. The relative received energy is plotted as a function of sphere depth on a semi-logarithm scale. Three excitation signals are considered. They are (1) a wideband excitation with carrier frequency 2.5 GHz, the resonant frequency of the sphere in the water medium, and pulse width 2.4 nsec (the case considered in the previous section); (2) a narrowband excitation with carrier frequency 1 GHz and pulse width of 1 μsec and (3) a narrowband excitation with carrier frequency 0.8 GHz and pulse width of 1 μsec. The latter two cases describe narrowband excitation signals where the medium-target exhibit maximum power transfer for the target located at 80 mm and 255 mm respectively.

The narrowband signal energy is an exponential function of sphere depth, as predicted by monochromatic electromagnetic wave propagation theory and as illustrated by the linear, semi-logarithmic curves in Figure 3.5. The lower carrier frequency monochromatic signal (0.8 GHz) when compared to the higher carrier frequency signal (1 GHz) has a smaller energy when the sphere is near the interface due to the decreased cross section of the sphere but decays less rapidly with sphere depth due to the narrowband propagation characteristics of the medium, as illustrated in Figure 3.2. The wideband signal has more energy when the sphere is near the surface because its carrier frequency corresponds to the sphere resonance in the water medium. Initially, the

signal energy of the wideband signal decays exponentially since the principal contribution to the signal energy is in the main lobe of the spectrum at the carrier frequency of 2.5 GHz. When the main lobe of the spectrum is attenuated beyond the low frequency sidebands, as illustrated in Figure 3.2, the wideband signal energy begins to decay in a non-exponential fashion, here approximately as $1/r_s^3$.

Figure 3.5 illustrates an important point and confirms the analysis above. For any sphere depth and known medium propagation properties, there is a narrowband excitation which produces greater energy at the output of the matched filter than the wideband excitation with carrier frequency at the resonance or largest cross section of the sphere. Thus, assuming the most sensitive matched filter processing of the received signal in additive white noise, there is a narrowband excitation which gives greater probability of detection of the target embedded in a dispersive water medium than does a wideband excitation.

The sensitivity of the response of a Debye medium due to the phase of the carrier was illustrated in the last section when we discussed the step response of the medium. For the problem considered here, changing the phase of the carrier signal of the excitation pulse so that the pulse contains partial sinusoids will create step discontinuities in the waveform at the leading and trailing edges of the pulse and thus increase the high frequency spectral content of the excitation. Also, partial cycles of the carrier that do not integrate to zero enhance the residual low frequency or DC content in the signal.

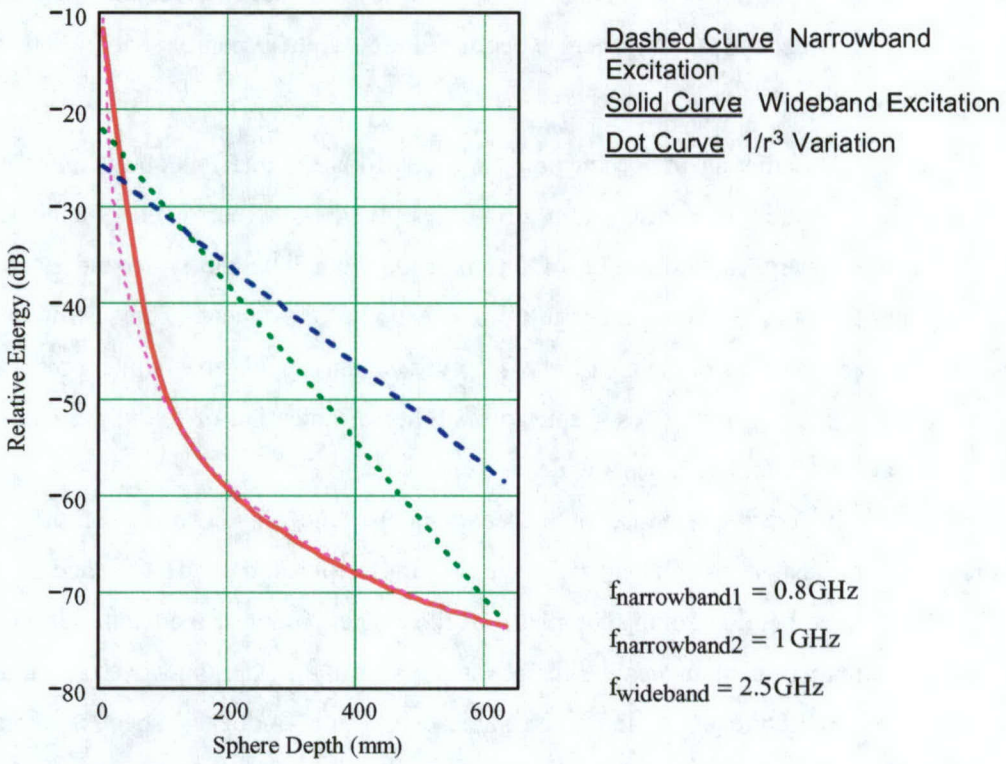

Figure 3.5. The relative received energy is plotted as a function of sphere depth. Three excitation signals are considered: (i) a wideband excitation with carrier frequency at 2.5 GHz and pulse width of 2.4 nsec; (ii) a narrowband excitation with carrier frequency at 1 GHz and pulse width of 1 μsec; and (iii) a narrowband excitation with carrier frequency at 0.8 GHz and pulse width of 1 μsec. The reference energy is from a free space sphere narrowband signal (1 msec pulsewidth) at 2.5 GHz (sphere resonance).

However, the model we have proposed here to characterize the radar scattering problem emphasizes the portion of the excitation signal in the passband between low frequency, Rayleigh scattering and high frequency medium attenuation. The model de-emphasizes power in the spectrum at low and high frequencies. Thus, under a constraint that the excitation has limited energy, discontinuities and partial cycles in the excitation affect the response primarily to the extent that they remove power from the bandpass frequencies that contribute primarily to "precursor-like" signal formation.

To illustrate this point, we have recomputed the relative energy in the reflected pulse from a sphere embedded in a Debye medium (Figure 3.5) for the cases when the excitation pulse contains 6, 6.25 and 6.5 carrier cycles. The results are shown in Figure 3.6. The solid curves give the relative energy response due to wideband excitation. The energy response differs by less

that 2.7 dB among the three partial cycle cases under the constraint that all excitation pulses have the same energy. Note that in the three cases considered, there are still narrowband excitations that result in greater received energy derived from concentrating the excitation energy in the passband generated by the medium attenuation and target Rayleigh scattering.

Thus, for detection of signal scattering in white noise, these results emphasize the importance for detection of signal scattering in white noise of concentrating available excitation signal in the target-medium passband where the total energy is attenuated least by the medium and the target. With limited excitation energy, wideband signal effects that distribute energy outside the pass band are deleterious to detection. Among these wideband signal effects are (1) placing the carrier outside the pass band, (2) creating step or near step discontinuities that create high frequency energy and (3) creating low frequency signal content that is not efficiently radiated or scattered.

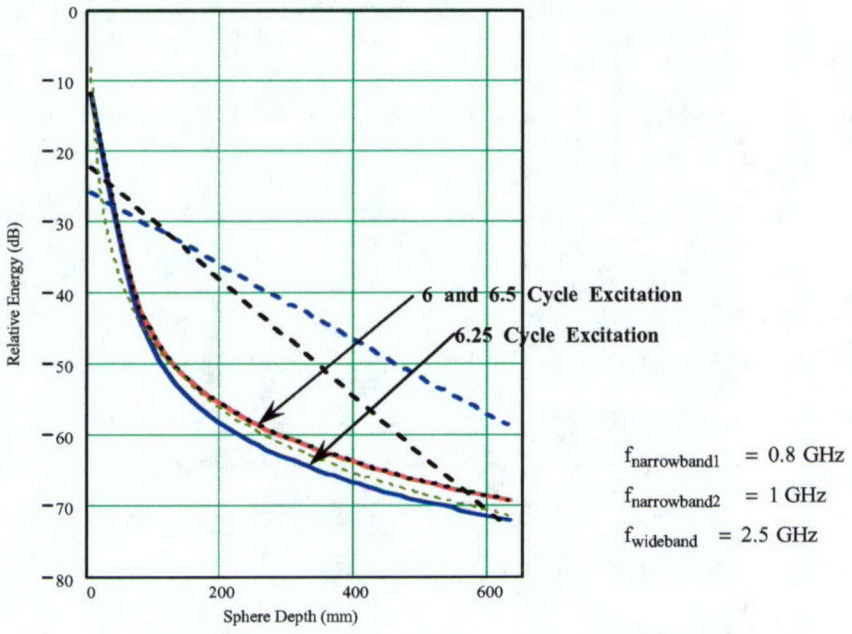

Dashed Curves -- Narrowband Excitation
Solid Curves -- Wideband Excitation with 6, 6.25 and 6.5 Cycles
Dot Curve -- $1/r^3$ Variation
Reference Energy: Energy from free space sphere with Narrowband Signal (1 msec pulsewidth) at 2.5 GHz (sphere resonance)

Figure 3.6. The relative received energy is plotted as a function of sphere depth. Three excitation signals are considered: (i) a wideband excitation with carrier frequency at 2.5 GHz and pulse width of 2.4 nsec; (ii) a narrowband excitation with carrier frequency at 1 GHz and pulse width of 1 μsec; and (iii) a narrowband excitation with carrier frequency at 0.8 GHz and pulse width of 1 μsec.

4. Ultra-Wideband Signal Propagation in Foliage

The problem of air or spaceborne radar detection of targets of military significance embedded in foliage is technically difficult. Microwave radar signals suffer significant foliage attenuation due to absorption and scattering losses in the random foliage medium. In addition, propagation dispersion in the random medium causes degraded signal coherence with angular and frequency changes, limiting radar signal processing capabilities for pulse compression and synthetic aperture image formation. Therefore, most foliage penetration radar designs contemplate operation in the VHF or UHF bands where foliage attenuation is less significant. However, longer wavelength radars are more difficult to design for ground clutter rejection and detection of slowly moving or stationary targets due to larger antenna beamwidths, less ability for antenna pattern control and limited bandwidth.

A foliage medium is composed largely of air. At most, approximately one tenth of one percent of the volume of natural foliage is composed of wood and leaves, which in turn exhibit frequency dependent electrical conduction and polarizability losses and which are a source of dispersion in foliage propagation. When the wavelengths of electromagnetic waves are large in comparison with the physical size of the constituents of the foliage, the waves propagate, on the average, according to the spatial average electrical properties of the foliage. Thus, the conduction and polarizability losses of tree wood and leaves create loss and dispersion in wave propagation. In this section, we discuss the frequency dispersion of electromagnetic waves in the VHF, UHF and lower microwave frequency bands, evaluate whether the dispersion produces significant ultra wideband radar waveform distortion and whether that distortion is useful for improved target detection.

4.1 Brown-Curry Model for Electromagnetic Wave Propagation in Foliage

Brown and Curry [Brown and Curry, 1980, 1982] have developed an analytical theory for electromagnetic wave propagation through foliage appropriate to VHF, UHF and lower microwave frequencies. The theory derives from (1) the Foldy-Twersky analysis of wave propagation through a sparse concentration of discrete, random objects [Ishimaru, Vol. II, 1978], (2) the scattering properties of discrete, dielectric Rayleigh objects, and (3) the physical and electrical properties of trees and their wood constituents. In the following, we briefly summarize

the theory developed by Brown and Curry for the average electromagnetic wave propagating in foliage in preparation for using this theory to evaluate the distortion of ultra-wideband electromagnetic signals by foliage.

The Foldy-Twersky theory provides the complex effective propagation constant of the average or coherent forward propagating electromagnetic field in a medium consisting of a sparse concentration of discrete, randomly positioned and oriented objects. Foliage is indeed such a medium. The fractional volume of wood components (branches and limbs) in forests is approximately 0.1% for mature forests, including jungles. Even in the extreme case of well-managed forests in Eastern Europe, the fractional volume is less than 0.5%. Leaves and needles compose less than 0.01% by volume of the forest and are very small scatters in the VHF and UHF bands.

The complex effective propagation constant based on the Foldy-Twersky theory is given as

$$k^2 = k_0^2 + 4\pi\rho\overline{f}_{k_0}(\overline{k}_i, \overline{k}_i)\cdot\hat{e}_i, \tag{4.1}$$

where $k = \omega/v$ is the effective wavenumber of the average field propagating inside the random medium, v is the propagation speed of the effective wave, and $k_0 = \omega/c$ is the wavenumber of free space. In (4.1), ρ denotes the average number of scatterers per unit volume, $\overline{f}_{k_0}(\overline{k}_i, \overline{k}_i)$ is the average forward scattering amplitude of a single object in free space, and $\hat{e}_i$ is the unit polarization vector of the incident electric field.

Brown and Curry have extended the Foldy-Twersky theory to media consisting of Rayleigh scatterers (small in comparison to the free space wavelength) with large loss. They considered the discrete objects to be tree trunks and branches and chose canonical shapes of long, thin dielectric cylinders to determine the forward scattering properties of the average object. The cylinder diameters were limited to $\lambda_0/2$ up to approximately 40 cm based on experimental observations by others. In the cylinders, material losses were considered to dominate in determining the effective wave number, although an ad hoc correction for scattering losses was included in the theory. Brown and Curry give the following expression for the effective wave number under these conditions

$$k^2 = k_0^2 + k_0^2\,\rho V_\rho(\varepsilon_r - 1)\,g(\varepsilon_r), \tag{4.2}$$

where ρV_ρ denotes the volume fraction of the medium occupied by the scattering objects, ε_r is the complex relative permittivity of the material in the scattering objects, and $g(\varepsilon_r)$ is the scalar ratio of the average interior field and average incident field on the object.

Applying Brown and Curry scattering results for long, thin and lossy dielectric cylinders, they found that for forests, the signal attenuation per unit length of the propagation path the coherent field is given approximately by

$$\text{Attenuation} = \text{Im}(k) \approx -k_0 (\rho V_\rho) q \left[\varepsilon_r'' + \frac{(\varepsilon_r' - 1)}{10} \right]. \tag{4.3}$$

Here q accounts for the polarization-limb/branch orientation; $q = 0.25$ for vertical polarization and skewed probability density for limb/branch orientation, $q = 0.125$ for horizontal polarization and skewed probability density, and $q = 0.167$ for both polarizations and uniform probability density.

n the expression (4.3), the first term, proportional to the imaginary part of the wood relative dielectric constant, ε_r'', accounts for material loss contributions to signal attenuation, while the second term, proportional to $\varepsilon_r' - 1$ (the deviation from free space of the real part of the relative dielectric constant), accounts for the signal attenuation due to scattering of the incident signal out of the forward propagation direction by the discrete, random objects. The latter term represents a bound (1/10) on the scattering losses and is applied in an ad hoc manner by Brown and Curry.

For purposes of analyzing the propagation of ultra-wideband signals in foliage, the frequency dependence of the signal attenuation is of particular importance. Figure 4.1 shows the frequency dependence of the fractional volume, ρV_ρ, used by Brown and Curry based on the wood density of trees in forests and limiting the limb/trunk diameter to 40 cm. Notice that the fractional volume is approximately 0.1% and has limited frequency dependence.

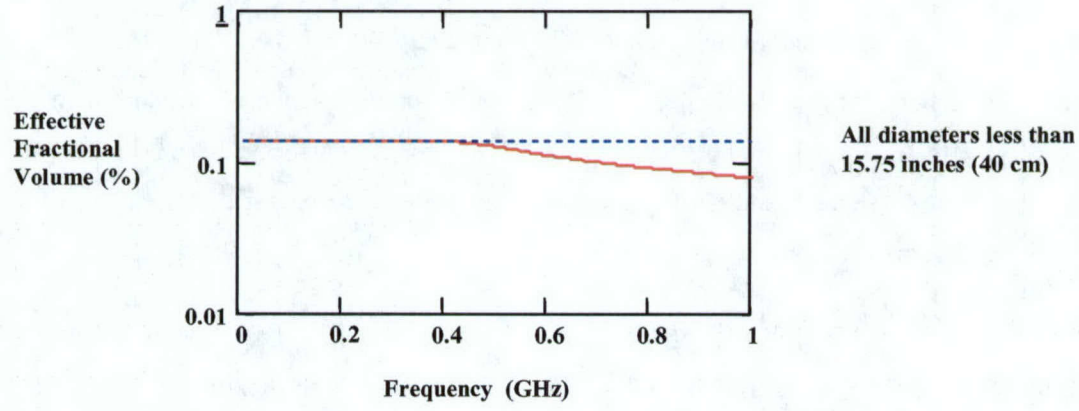

Figure 4.1. The fractional volume of forest (%) composed of limb and trunk wood material that contributes to wave attenuation as a function of wave carrier frequency.

Thus, the principal frequency dependence of the signal attenuation derives from the frequency dependence of the relative permittivity ε_r. Based on studies of experimental data, Brown and Curry concluded the following properties of the relative permittivity: (1) the real part of the dielectric constant, ε_r' , is constant at frequencies above 20 MHz and depends on the moisture content and temperature of the wood. However, typical values for dielectric constant are,

$$\begin{aligned} &30 < \varepsilon_r' < 68 \qquad \textit{E Field Parallel to Wood Grain} \\ &13 < \varepsilon_r' < 54 \qquad \textit{E Field Perpendicular to Wood Grain,} \end{aligned} \tag{4.4}$$

and (2) the imaginary part of the dielectric constant, ε_r'' ,has significant frequency dependence due to conduction and polarization losses of the wood moisture. Based on experimental data

$$\varepsilon_r'' = \frac{A}{f^{0.96}} + \frac{B\dfrac{f}{f_c}}{1+\left(\dfrac{f}{f_c}\right)^2}; \tag{4.5}$$

where the resonant frequency f_c depends on season and is given by

$$f_c \cong \begin{cases} 20\,\text{GHz} & \textit{Summer} \\ 10\,\text{GHz} & \textit{Winter} \end{cases}; \tag{4.6}$$

the coefficient A depends on polarization and is given as

$$A \cong \begin{cases} 1.5\times10^9 & E_{parallel} \\ 4\times10^8 & E_{perpendicular} \end{cases}; \tag{4.7}$$

the coefficient $B = B(\textit{Moisture Content})$ is a function of moisture content in wood as given in Figure 4.2.

In the expression for the imaginary part of the effective dielectric constant of foliage, (4.5), the first term represents an approximation to conduction losses while the second term accounts for polarizability losses. The conduction losses are due to ionic conduction due to salts and minerals in the tree sap and dominate below approximately 600 MHz. The conduction losses have approximate $1/f$ frequency dependence and depend on the polarization of the incident electric field with respect to the grain of the wood fibers via the factor A. Note that the conduction losses are higher for the cases when the incident electric field is parallel to the wood

grain. The polarizability losses dominate above 600 MHz. They model the dipolar relaxation of the water in the wood and thus depend on the moisture content of the wood via the factor B, as given in Figure 4.2, and the temperature of the wood fibers. The polarization resonant frequency, f_c, is near that of water when the wood is warm but is reduced to approximately 10 GHz when the wood is near freezing or below. The polarization losses due to wood polarizability are assumed to be independent of the polarization of the incident field.

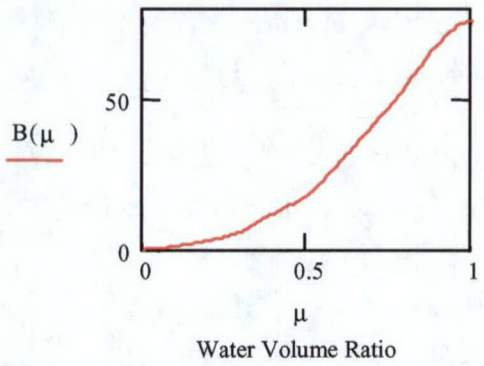

Figure 4.2. Coefficient B for Debye losses in wood as a function of water volume ratio.

Figure 4.3 shows the real and imaginary parts of the effective dielectric constant predicted for foliage from the Brown-Curry model (dashed curve) in comparison with the model applied in [Oughstun, 2001] with smaller losses (solid curve). Note that the Brown-Curry model predicts that the real part of the dielectric constant for the foliage is near one at 600 MHz, consistent with the observation earlier that wood fiber occupies less that 0.1% of the forest volume. Also, the imaginary part of the dielectric constant is dominated by conduction losses, as exhibited by the $1/f$ behavior up to approximately 600 MHz. In comparison, the low loss case (solid line) shows linear frequency behavior in the VHF and UHF frequency bands. This is typical of water as observed in the previous section of this report.

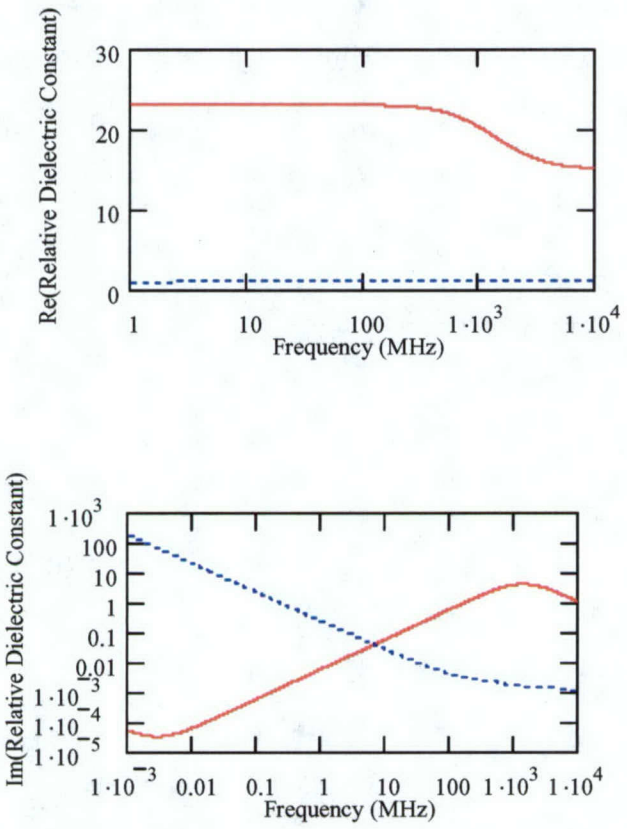

Figure 4.3 Real and Imaginary parts of the effective dielectric constant of foliage predicted by Brown and Curry model (dashed curve) and the model applied in [Oughstun, 2001] (red solid curve).

Figures 4.4 and 4.5 show the respective propagation phase and attenuation in foliage as a function of frequency predicted using the Brown-Curry model. As shown in Figure 4.4, the phase has approximately linear frequency dependence, giving pure time delay of the signal. The attenuation as a function of frequency in Figure 4.5 is of particular interest for the possible formation of precursors in foliage. At low frequencies, about 1 to10 MHz, the attenuation has little frequency dependence. On the other hand, at frequencies above about 500 MHz, the attenuation varies approximately linearly with frequency. This corresponds to other models for foliage attenuation compiled by MIT Lincoln Laboratory [Mower, 1988, Bessette and Ayasli, 2001] and based on a number of field experiments over the last 30 years. At low frequencies and high frequencies, the attenuation is dominated by the absorption losses associated with the wood properties of the trunks and limbs. Only at the transition band, approximately from 100 to 600 MHz, do the scattering losses, as bounded in the model and associated with the scattering from the assumed Rayleigh cylinders, become comparable to the absorption losses. These results were

computed for parameters that emphasize the Debye polarization losses over conduction losses and are thus optimistic from the viewpoint of precursor formation in the foliage medium. Specifically, the parameters are $\varepsilon_r' = 30$, $A = A(E_{perp}) = 4\times10^8$, $\mu\rho = 0.75$, $B = 47.2$, $q = q(Hpol, skewed) = 0.125$, $f_c = f_c(winter) = 10\,\text{GHz}$.

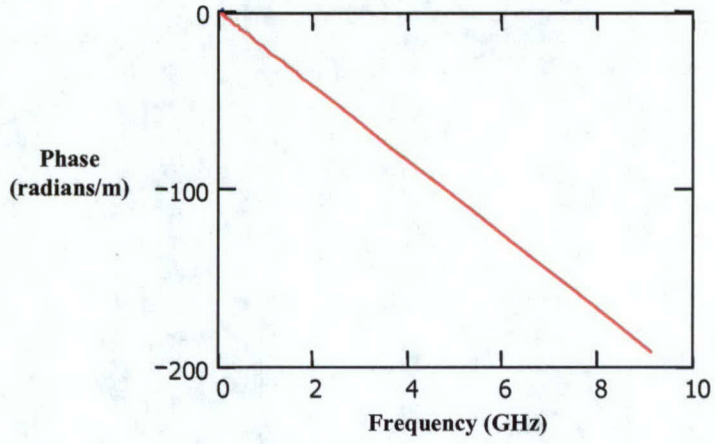

Figure 4.4. Predicted wave propagation phase in foliage as a function of frequency using the Brown and Curry model.

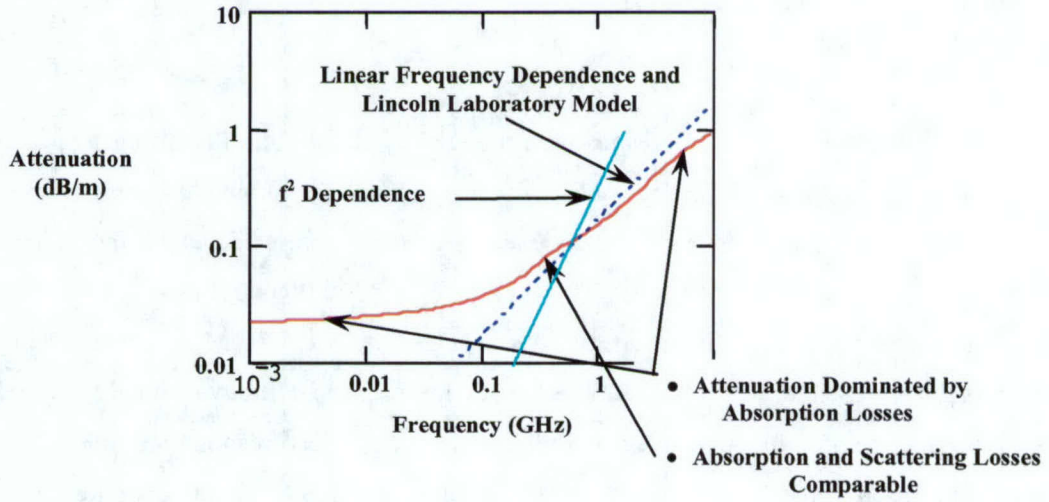

Figure 4.5. Predicted wave propagation attenuation in foliage as a function of frequency using the Brown and Curry model (red solid curve). The linear frequency dependence of attenuation is shown as the dashed blue curve, and the squared frequency dependence of attenuation is the blue solid curve.

The values of ε_r' and ε_r'' used in these calculations are taken independently from equations 4.4 and 4.5, respectively. These equations for the complex relative dielectric constant are based on experimental observations of wood dielectric properties and as such do not necessarily obey the Kramers-Kronig relations which guarantee causality in the field response.

To investigate this potential problem, the imaginary part of the relative dielectric constant, ε_r'', as given by equation (4.5) with the parameters given before Figure 4.4 was numerically fit to the imaginary part of equation (2.5) with $\varepsilon_s = 50$ and $\sigma = 44 millimho/m$ [Oughstun, 2001]. The results of this fit are shown in Figure 4.6.

There is a very good fit between the experimental Brown-Curry model for the imaginary part of the wood relative dielectric constant and the causal model. The real part of the relative dielectric constant as given by the causal model differs significantly from the constant dielectric constant selected from the Brown-Curry model. For carrier frequencies below 1 GHz, the real part of the relative dielectric constant is increased 70%. Above 1 GHz, the real part shows significant frequency dependency, decreasing to the assumed free space value above the Debye resonance frequency of 10 GHz.

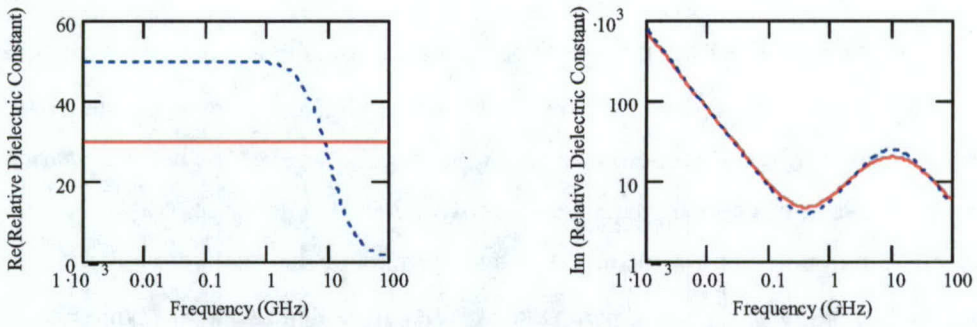

Figure 4.6. Comparison of the Brown-Curry model with imposed causality. Solid curves are the Brown-Curry model and the dashed curves are the result of imposing causality.

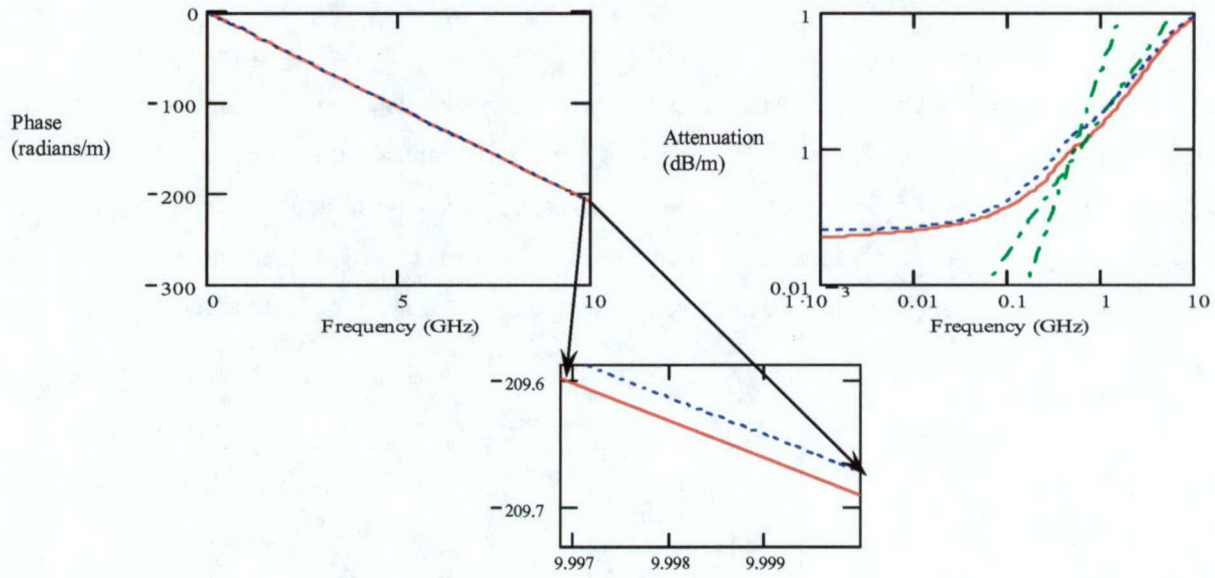

Figure 4.7. Comparison of the phase and attenuation per unit of propagation direction with the Brown-Curry parameters and the causal approximation to the Brown-Curry dielectric model.

Figure 4.7 compares the phase and attenuation of foliage as determined from equation (4.3) with the Brown-Curry parameters and the corresponding causal model. There is negligible change in the phase. The maximum deivation is 0.02 radian/meter at 10 GHz. The phase variation with frequency remains essentially linear and this change implies a slight change in the estimated delay of the response waveform. The attenuation of the foliage medium increases slightly at frequencies below 1 GHz when compared with the Brown-Curry model parameters. This is due to increased scattering losses caused by the increased real part of the wood dielectric constant for the causal model of the wood dielectric constant. For frequencies above approximatly 500 MHz, the attenuation increases at a rate which is more nearly linear with frequency than as the square of frequency as occurs in the highly dispersive water medium.

4.2 Ultra-Wideband Electromagnetic Field Propagation in Foliage

We turn now to the study of ultra-wideband electromagnetic field propagation in foliage. As observed previously, the foliage medium has random propagation parameters, determined by the random shape, orientation and material properties of the tree trunks, limbs and leaves. The Brown–Curry model for field propagation describes the ensemble average field, where averaging has been accomplished over the random foliage properties. We will study the properties of this ensemble average or coherent field under the assumption of ultra-wideband excitation of the medium.

We consider a slab of foliage that is 25 meters thick and has average propagation characteristics which emphasize Debye losses over conduction losses in the foliage and which are illustrated in Figure 4.5. We observe the field at a distance that is 3 meters beyond the slab. For this medium, the slab is 1.74 skin depths thick at a carrier frequency of 5 GHz. For these calculations, we consider only one-way propagation and neglect multiple reflections between the diffuse air-foliage interfaces.

Figure 4.8 shows the spectrum of a five cycle, ultra-wideband signal with carrier frequency of 5 GHz and pulse width of 1 nsec before and after one-way propagation through the slab of foliage. The dashed curve represents the magnitude squared of the medium transfer function. Note that in Figure 4.8 the spectrum of the output signal has the following properties:

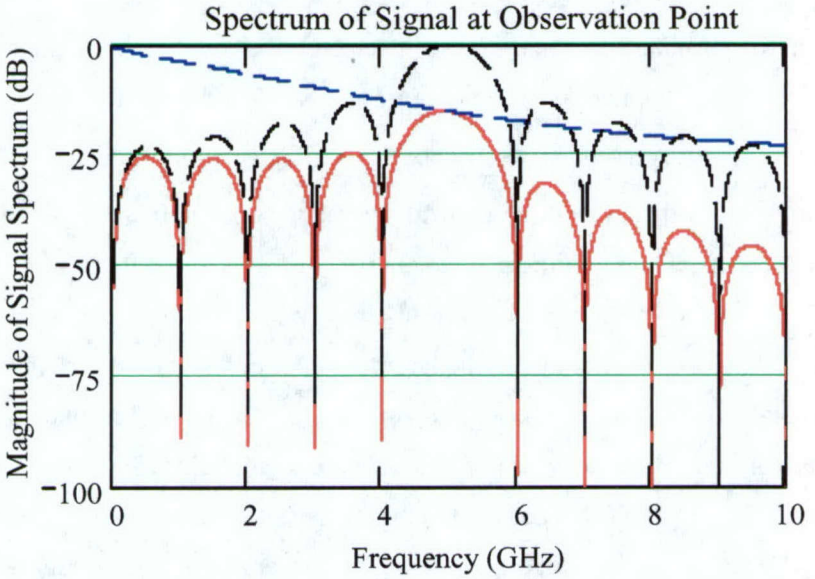

Figure 4.8. The spectra of the excitation signal with carrier frequency of 5 GHz and pulse width of 1 nsec (black dashed curve), the magnitude squared of the foliage medium transfer function (blue dashed curve), and the signal at the observation point

(1) A large contribution to the power in the signal comes from the main lobe of the spectrum around 5 GHz. This is unlike the case of water where the attenuation increases as f^2 and where the main lobe of the spectrum is greatly attenuated with respect to the low frequency sidebands of the signal.

(2) The low frequency sidebands of the signal after propagation through the foliage slab are equalized in power by the foliage transmission function at a level that is approximately 10 dB below the peak of the spectrum.

(3) The high frequency sidebands are attenuated at a rate greater than the $1/f^2$ intrinsic to the excitation signal spectrum due to the increasing foliage attenuation with frequency. However, the roll-off is not as great as was observed in water where the Debye losses are more prominent.

The time responses of the coherent or ensemble average signals observed after foliage slab propagation and the signal propagated in free space are illustrated in Figure 4.9. These results were computed numerically using the discrete Fourier transform representation of the signal spectrum of Figure 4.8 after propagation through the foliage slab and with time delay associated with free space propagation. These curves give the analytic signal representation of the observed signal, emphasizing the temporal amplitude and phase modulation of the 5 GHz carrier frequency. The envelope represents the amplitude modulation and the quadrature components are the real and imaginary parts of the amplitude and phase modulation in polar representation.

The signal propagated through the slab is dominated by carrier frequency contributions with weak or little precursor formation. This can be traced to the weak (approximately linear) frequency dependence of the attenuation illustrated in Figures 4.5 and 4.7. This is in contrast to the strong (f^2) dependence observed in water. The weak frequency dependence of attenuation can be traced further to the foliage model of Brown and Curry. In the Brown-Curry model we observed that conduction losses due to the ionic conductivity of salts and minerals in the tree sap dominated polarizability or Debye losses. Thus in foliage we lose much of the Debye behavior that is the source of precursors in water due to the domination of conduction losses in foliage and the small fractional volume of the foliage medium occupied by trunks, branches and leaves. Demanding that the real and imaginary parts of the wood relative dielectric constant satisfy the Kramers-Kronig relations (Figure 4.6) does not change this conclusion since the frequency dependence of foliage medium attenuation remains essential linear as pictured in Figure 4.7.

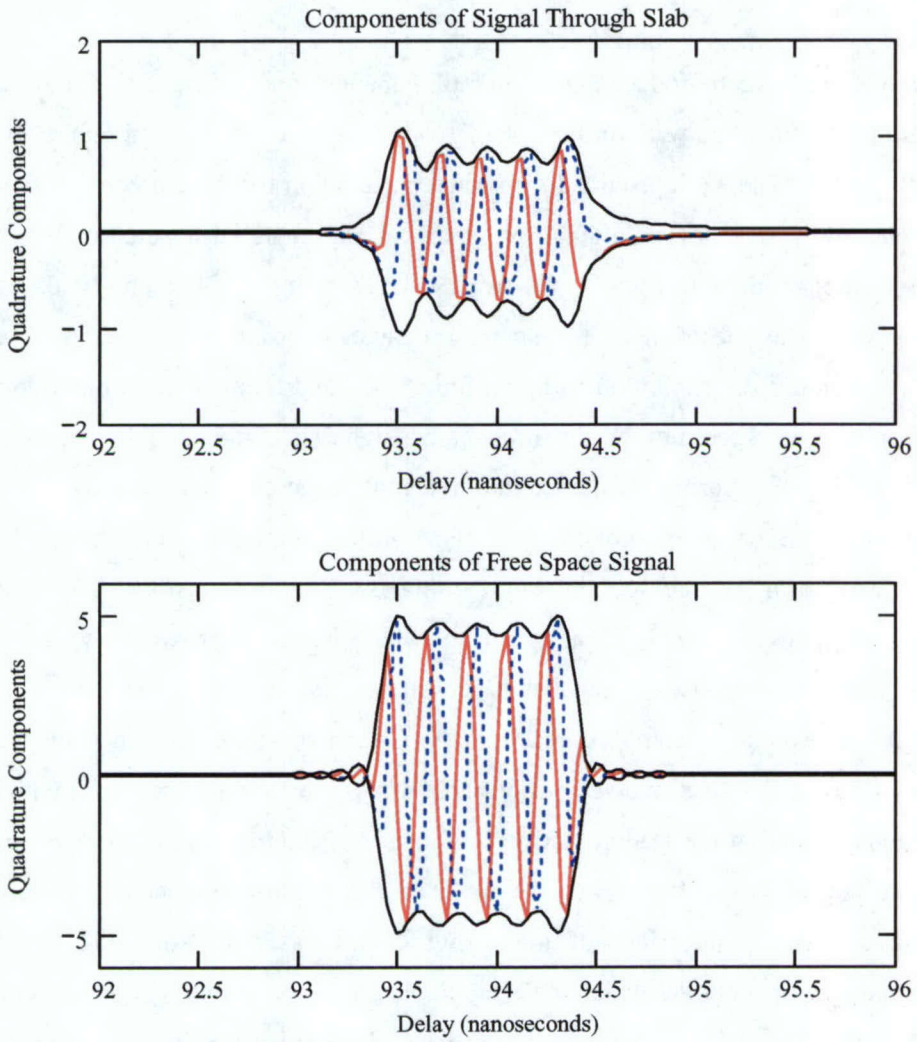

Figure 4.9. The time responses of the coherent average signals observed after foliage slab propagation and the signal propagated in free space.

5. Summary and Conclusions

In this work, we have reproduced the work of Albanese and others that demonstrate the formation of precursor-like waveforms when water is excited by an ultra wideband electromagnetic wave. The work provided a physical explanation for these precursor waveforms. The Debye characterization of polarizability losses in the material results in very rapidly increasing wave attenuation with frequency in those bands where the polarizability losses exceed conduction losses. The spectrum of the signal propagated through the medium is changed dramatically. Assuming the excitation to be an ultra wideband modulated carrier frequency (a few carrier cycles), the spectrum of the propagated signal is dominated by equalized, low frequency sidebands. The portion of the excitation signal at the carrier frequency and above is greatly attenuated. Because of the linearity of Maxwell's equations and the medium, the precursor-like waveform can be found from the inverse Fourier transform of the complex spectrum of the propagated signal. That spectrum, when viewed approximately as a constant (boxcar) over the lower frequency sidebands of the excitation multiplied by the sinusoid associated with the excitation complex spectrum, results in the time domain response as the convolution of a short pulse (the inverse Fourier transform of the constant spectrum) with impulse or delta functions located at the leading and trailing edges of the excitation (the inverse Fourier transform of the sinusoidal spectrum modulation). Thus, the precursor like behavior is associated with the leading and trailing edges of the response and has a duration that is inversely proportional to the bandwidth over which the excitation signal is equalized by the medium.

In this work, we have demonstrated the properties of these precursor-like waveforms that are important if these waveforms are to be considered for radar detection of targets embedded in foliage. These properties are:

(1) Precursor-like waveforms are greatly attenuated. This is due to the fact that the precursor formation medium must be highly dispersive and demonstrate rapidly increasing attenuation with frequency. The precursor-like waveforms are formed from sideband energy of the excitation in a medium that has greatly attenuated the carrier frequency and upper sideband energy.

(2) Precursor-like behavior is exhibited only after propagation through several skin depths of the medium at the carrier frequency of the excitation. This insures that the carrier and upper sidebands of the excitation are greatly attenuated.

(3) Precursor-like behavior of the response waveform persists with target scattering when the target is embedded in a dispersive, Debye medium. Target scattering attenuates low frequency portions of the spectrum due to Rayleigh scattering from the target at very low frequencies. As long as there remains a substantial portion of the response spectrum that is equalized over a band between the Rayleigh scattering and the carrier frequency, the precursor-like behavior of the time response will be observed. In this case, the duration of the precursors will be increased due to the low frequency bandwidth limitations imposed on the spectrum by the target Rayleigh scattering.

The low frequency attenuation of Rayleigh target scattering is a proxy for a number of low frequency limitations on air or spaceborne radar. Specifically, for any limited size transmit/receive antenna as would be appropriate for air or spaceborne radars, antenna gain decreases at very low frequencies, thus reducing radar sensitivity to the lower frequency components of the radar signal. Also, ground targets, when viewed at small grazing angles, exhibit target-earth interaction characterized most simply in terms of multipath interference between the target and its image in the earth. The small grazing angle multipath effects become more prominent at low frequencies where the earth's surface becomes more specular and more greatly attenuates the resultant signal from the target.

(4) Foliage is weakly dispersive when compared to water and results in weak or negligible precursor formation in the coherent or ensemble average waveform at reasonable foliage depths. According the experimental observations of trees and their wood fibers, as modeled by Brown and Curry, wood conductivity due to the ionic conductivity of salts and minerals in the tree sap dominate Debye losses. The component of loss associated with Debye polarizability resonance is sensitive to water content of the wood and the resonant frequency is between 10 and 20 GHz, depending on the temperature of the wood. Since conductivity dominates, we lose much of the Debye behavior that is the source of precursors in water.

Finally, we considered the problem of detecting the scattered signal from a target embedded in a dispersive, Debye medium when the scattered signal is observed in additive, white noise. Classical detection theory directs that the received signal be processed in a filter matched to the precursor-like scattered signal and the filter observed at the time of peak response. The peak response is proportional to the total energy contained in the precursor-like scattered signal. More fundamentally, we determined the excitation or radar transmitted signal which, for a given target and dispersive medium, gives the greatest received energy. All designs of the transmitted signal were constrained to have the same energy.

We determined that the greatest target detectability resulted from concentration of the transmit signal energy in the band where the medium/target power transfer function is a maximum. We compared several excitations including an ultra wideband excitation at a high carrier frequency (UWB–HCF) at the resonant frequency of the target and narrowband excitations with smaller carrier frequencies (NB-LCF) into the Rayleigh region of the target. The UWB-HCF energy decays exponentially with target depth at small depths into the medium where the signal energy is dominated by the carrier frequency energy. At greater depths, the UWB-HCF energy has slower, non-exponential decay. On the other hand, the NB-LCF energy decays exponentially over the corresponding target depths since the skin depth of the medium at the lower carrier frequencies is greater. We demonstrated that there is always a narrow band signal at a lower carrier frequency that reflects greater energy than the ultra wideband signal at a higher carrier frequency, in spite of the exponential decay of energy and small scattering of the narrow band signal.

Thus, we conclude that when the radar design addresses solely detection in additive receiver noise that is white, the superior excitation for detection of a target in a dispersive medium is a narrow band signal with carrier frequency at the maximum of the target-medium power transfer function.

Indeed, practical experience with airborne, lookdown radars for detecting ground targets in foliage indicates that signal to noise and foliage attenuation are not the principal problems. Rather, false alarms from ground reflections appearing as targets is the more substantial problem. Air and spaceborne lookdown radars must minimize ground reflections sufficiently by the use of antenna and signal processing designs so that target signals may be detected in the ground reflection background. In either airborne, moving target detection radars that use target/ground relative Doppler shift to detect targets or synthetic aperture mapping radars that use target images for detection, short pulse or ultra wideband excitation signals may be useful to limit total ground reflections or to provide greater resolution in images. Indeed, the greater resolution can provide increased data by which improvements in target/clutter discrimination and target classification can be achieved.

6. Acknowledgements

The Air Force Office of Scientific Research (AFOSR) provided the funding of this project through task 01SN02COR managed by Dr. Arje Nachman. We would like to extend our gratitude to the following people at the Air Force Research Laboratory (AFRL), Hanscom AFB, MA for their interest, technical assistance and discussions: Drs. Peter Franchi, Robert Mailloux, Robert McGahan, Thomas Roberts, and Hans Steyskal. In addition, we would like to thank Dr. Richard Albanese and Prof. Kurt E. Oughstun for their comments. Discussions with Professor Gary Brown of the Electrical and Computer Engineering Department, Virginia Polytechnic Institute and State University, Blacksburg VA were especially useful in understanding foliage propagation models.

7. References

R. Albanese, J. Penn, and R. Medina, "Short-Rise-Time Microwave Pulses Propagation through Dispersive Biological Media," J. Opt. Soc. Am. A., Vol. 6, pp. 1441--1446, 1989.

C.A. Balanis, Advanced Engineering Electromagnetics, John Wiley and Sons, 1989, pp. 650-658.

T.W. Barrett, "Energy Transfer & Propagation and the Dielectrics of Materials: Transient versus Steady State Effects," in Ultra-Wideband Radar: Proc. 1st Los Alamos Symp., pp. 1-19, 1990.

L.A. Bessette, and S. Ayasli, UHF (P-3 UWB) and VHF (CARABAS II) Foliage Attenuation and Backscatter Measurements, MIT Lincoln Laboratory Project Report FPR-13, 18 October 2001.

J.G. Blaschak, and J. Franzen, "Precursor Propagation in Dispersive Media from Short-Rise-Time Pulses at Oblique Incidence," J. Opt. Soc. Am. A., Vol. 12, pp. 1501-1512, 1995.

L. Brillouin, "Uber die Fortpflanzung des Lichtens in Dispergierenden Medien," Ann. Phys., Vol. 44, pp. 203-240, 1914.

L. Brillouin, Wave Propagation and Group Velocity, Academic Press, New York, 1960.

G.S. Brown, and W.J. Curry, An Analytical Study of Wave Propagation through Foliage, RADC TR 79-359, ADA084348, Jan 1980.

G.S. Brown, and W.J. Curry, "A Theory and Model for Wave Propagation through Foliage," Radio Sci., Vol. 17, pp. 1027-1036, 1982.

C. Fowler, J. Entzminger, and J. Corum, "Assessment of Ultra-Wideband (UWB) Technology," IEEE AES Magazine, Nov., pp. 45-49, 1990.

C.W. Helstrom, Elements of Signal Detection and Estimation, PTR Prentice Hall, 1995, pp. 104-113.

A. Ishimaru, Wave Propagation and Scattering in Random Media, Vol. II, Academic Press, 1978.

J. D. Jackson, Classical Electrodynamics, Wiley, New York, 1975.

J. A. Kong, Electromagnetic Wave Theory, John Wiley and Sons, New York, 1990.

T. Mower, A Brief Summary of Foliage Attenuation Investigations, MIT Lincoln Laboratory Project Memo No. 46PM-STD-0001, October 1988.

A. Nachman, "A New Approach to an Old (Radar) Signal," AFOSR Research Highlights, Sep-Oct, 2001.

A.V. Oppenheim, A.S. Willsky, and S.H. Nawab, Signals and Systems, 2nd ed., Prentice Hall, Upper Saddle River, 1997.

K.E. Oughstun, "Pulse Propagation in a Linear, Causally Dispersive Medium," Proc. IEEE, Vol. 79, pp. 1379-1390, 1991.

K.E. Oughstun, and J.E.K. Laurens, "Asymptotic Description of Ultrashort Electromagnetic Pulse Propagation in a Linear, Causally Dispersive Medium," Radio Sci., Vol. 26, pp. 245-258, 1991.

K.E. Oughstun, and G.C. Sherman, Electromagnetic Pulse Propagation in Causal Dielectrics, Springer-Verlag, Heidelberg, 1995.

K.E. Oughstun, Foliage Penetration Using the Brillouin Precursor, Technical Memorandum, 22 May 2001.

OSD/DARPA Ultra-Wideband Radar Review Panel, Assessment of Ultra-Wideband (UWB) Technology, Battelle Tactical Technology Center, July 13, 1990.

A. Papoulis, The Fourier Integral and its Applications, McGraw-Hill, New York, 1987.

T.M. Roberts, and P.G. Petropoulos, "Asymptotics and Energy Estimates for Electromagnetic Pulses in Dispersive Media," J. Opt. Soc. Am. A., Vol. 13, pp. 1204-1217, 1996.

P.D. Smith, and K.E. Oughstun, "Electromagnetic Energy Dissipation and Propagation of an Ultrawideband Plane Wave Pulse in a Causally Dispersive Dielectric," Radio Sci., Vol. 33, pp. 1489-1504, 1998.

A. Sommerfeld, "Uber die Fortpflanzung des Lichtens in Disperdierenden Medien," Ann. Phys., Vol. 44, pp. 177-202, 1914.

J. A. Stratton, Electromagnetic Theory, McGraw-Hill, New York, 1941.